Mechanisms and implications of high depolarization baseline offsets in conductance-based neuronal models

Anal Kumar[1], **Anzal K. Shahul**[1], **Upinder S. Bhalla**[1,2]
[1]National Centre for Biological Sciences, Tata Institute of Fundamental Research, Bellary Road, Bangalore 560065, India
[2]bhalla@ncbs.res.in

Abstract

Somatic current-step injection is a routinely used protocol to characterize neurons and measure their electrophysiological properties. A signature feature of the responses of many neuronal types is an elevated baseline of action potential firing from the resting membrane potential, the depolarization baseline level offset (DBLO). We find that four key factors together account for high DBLO: Liquid Junction Potential correction, subthreshold impedance amplitude profile, fast potassium delayed rectifier kinetics, and appropriate transient sodium current kinetics. We show that simple mechanisms for DBLO, such as Ohmic depolarization due to current input, fail to explain the effect, and many sophisticated conductance-based models also do not correctly manifest DBLO. Neither low pass filtering effect of membrane nor high reversal potential of potassium channels are able to explain high DBLO. Using stochastic parameter search in conductance-based models of CA1 pyramidal neurons, we explore cellular morphology configurations and channel kinetics. Multi-compartment models which matched experimental subthreshold impedance amplitude profiles had higher DBLO than single compartment models. DBLO was further increased in models that exhibited rapid deactivation time-constants in the dominant potassium conductance. We also saw that certain transient sodium current kinetics resulted in higher DBLO than others. We emphasize that correct expression of DBLO in conductance-based models is important to make quantitative predictions about the levels of ion channels in a neuron and also to correctly predict mechanisms underlying cellular function, such as the role of persistent sodium in imparting firing bistability to a neuron.

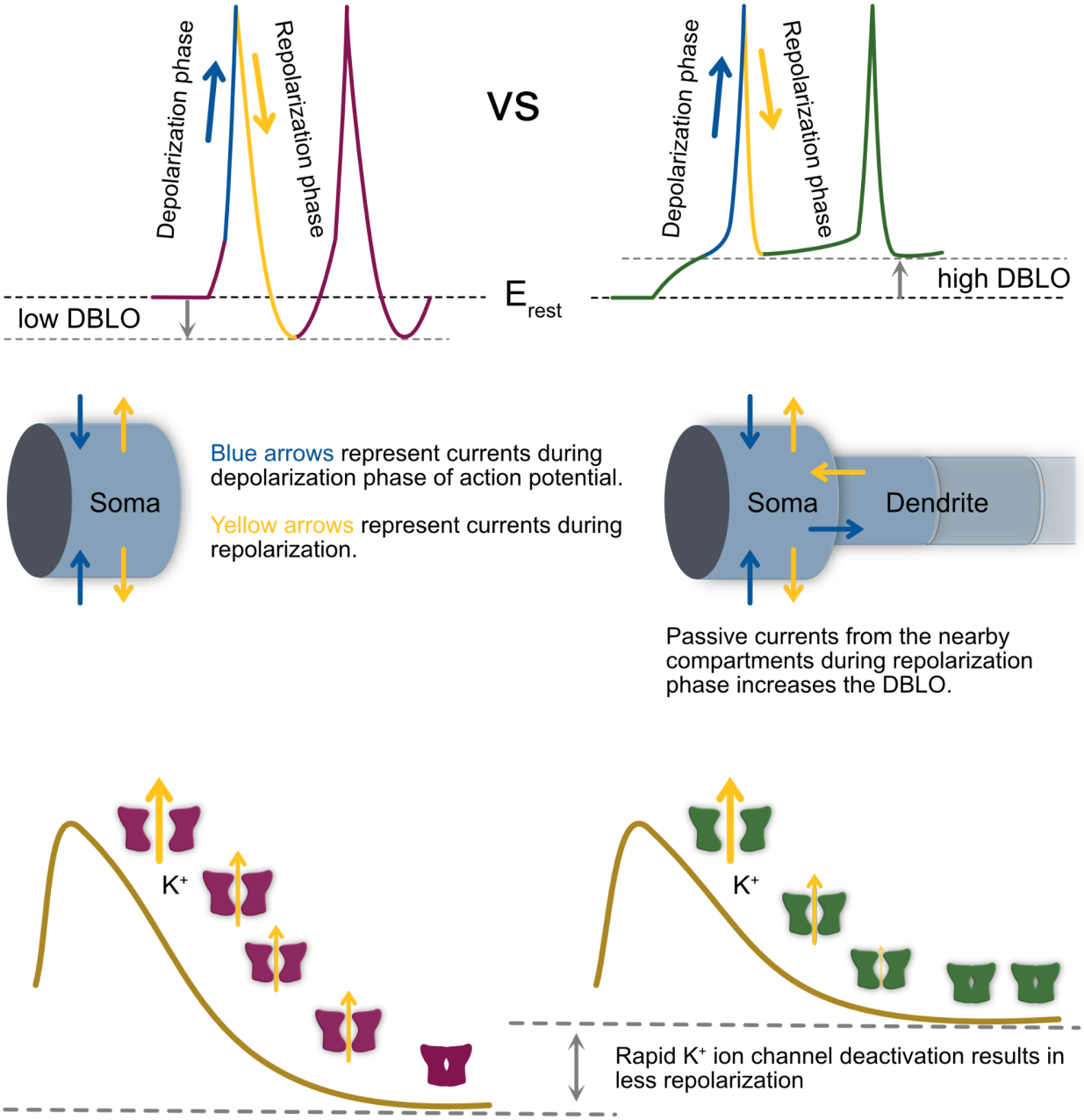
Depolarization phase
Repolarization phase
VS
Depolarization phase
Repolarization phase
low DBLO
E rest
high DBLO
Soma
Blue arrows represent currents during depolarization phase of action potential.
Yellow arrows represent currents during repolarization.
Soma
Dendrite
Passive currents from the nearby compartments during repolarization phase increases the DBLO.
K+
K+
Rapid K+ ion channel deactivation results in less repolarization

Glossary

AHP: Afterhyperpolarization
AIS: Axon Initial Segment
AP: Action Potential
CM: Specific capacitance
DBL: Depolarization Baseline
DBLO: Depolarization Baseline Offset
Eglu: Reversal potential of Glutamatergic ion channels
EK: Reversal potential of K^+ channels
ENa: Reversal potential of Na channels
E_{rest}: Resting membrane potential
E_{rev}: Reversal potential
Gbar: Maximal conductance
HCN: hyperpolarization-activated cAMP dependent channel
HH: Hodgkin-Huxley
K_DR: Delayed rectifier potassium channel
Na_P: Persistent sodium channel
Na_T: Transient sodium channel
RA: Axial resistance
Rin: Input resistance
RM: Specific membrane resistance
SA: Sino-Atrial
Tau: Time constant

Introduction

Accurate neuronal models have become a core part of experimental as well as computational neuroscience. Key details of action potential shape provided early clues about the existence and roles of various ion channels in different cell types. For example, the afterhyperpolarization (AHP) following an action potential in the sinoatrial (SA) node of the heart led to the discovery of funny (HCN) channels (Brown et al., 1979). Although extant neuronal models have been instrumental in providing insights into the biophysics of neurons, e.g. in understanding back propagating action potentials (M. Migliore et al., 1999) and calcium spikes (Miyasho et al., 2001), some key details have remained understudied. One such detail is the high Depolarization BaseLine Offset (DBLO) seen in somatic recordings when long pulses of current are injected into a neuron (Bianchi et al., 2022). High DBLO can be seen in current clamp recordings of almost all pyramidal neuron subtypes: hippocampal CA1 (Dwivedi et al., 2019), CA3 (Hunt et al., 2018), cortical L2/3 (Moradi Chameh et al., 2021) and L5 (Kim et al., 2015; Moberg & Takahashi, 2022). Many other neurons, including thalamocortical neurons (Studtmann et al., 2023), and olfactory bulb M/T cells (Fadool et al., 2011) also exhibit high DBLO. Neurons with low DBLO include fast-firing basket cells (Pawelzik et al., 2003; Szabó et al., 2010). Notably the original Hodgkin-Huxley squid channels generate low DBLO (Hodgkin & Huxley, 1952), and this has tended to dominate illustrations of neuronal firing ("Action Potential," 2023; Kandel et al., 2021). Since high DBLO is also seen in perforated patches (Hess et al., 2021; Staff et al., 2000), and opsin induced stimulations (Alejandre-García et al., 2022), it is unlikely to be a method-specific phenomenon.

Several studies have hinted at a role of morphology in the phenomenon of high DBLO . Pinching or cutting off dendrites leads to disappearance of high DBLO (Bekkers & Häusser, 2007). Furthermore, a modeling study (Hendrickson et al., 2011) showed that high axial currents from dendrites resulted in a reduction in the amplitude of fAHP which is a proxy of high DBLO in these spontaneously firing neuron models. It can be argued that a sustained depolarizing current can give rise to high DBLO. However, blocking persistent sodium channels (Na_P) does not lead to low DBLO (Müller et al., 2018). Calcium channels also do not seem to have a significant effect on DBLO as blocking Ca channels or changing Ca^{+2} levels had limited effect on fAHP and thus DBLO (Sahu et al., 2017, 2019). Further, blocking R type Ca channels also did not have a significant effect (Metz et al., 2005).

This phenomenon of high DBLO has been largely ignored by modelers. As we analyze below, several models of CA1 pyramidal neurons on ModelDB do not show the experimentally expected level of DBLO upon current clamp. Recently, Bianchi et al., 2019 addressed this issue and suggested that the high Depolarization Baseline may be due to an injection-current dependent shift in reversal potential on ion channels as well as their kinetics (Bianchi et al., 2022). The mechanistic basis for such a proposed current-dependent shift is uncertain.

With current morphological (Ascoli et al., 2007; Gouwens et al., 2018) and ion channel (Podlaski et al., 2017; Ranjan et al., 2011) databases, and easy access to powerful computers and simulators (Alam et al., 2022; Carnevale & Hines, 2006; Eppler et al., 2009; Goodman & Brette, 2008; Ray & Bhalla, 2008), it is easy to build complex models which may in some cases avoid errors in model behavior without providing insights into what went wrong. This is pronounced if a phenomenon is a composite outcome of multiple mechanisms, which, as we

find, is the case for DBLO. Thus we found it valuable to work through minimal models to pin down individual mechanistic contributions. To do this, we systematically checked the contributions of various factors in conductance based models of CA1 pyramidal neurons that affect DBLO and contribute to high DBLO.

In the current study, we obtained electrophysiological data from mouse CA1 pyramidal neurons for passive properties, frequency response, and DBLO with current clamp recordings. We used this data to build models and to explore factors that affect DBLO. We found out that multiple factors contribute to DBLO, including passive properties, morphology, and channel kinetics. Notably, physiological DBLO was not possible in a single compartment model of a neuron using default channel kinetics. Multicompartment models with experimentally constrained subthreshold impedance amplitude profiles were required to get higher DBLO than single compartment models. However, DBLO levels could be increased in a single compartmental model when a primary potassium channel with sufficiently small deactivating time constant was used. Additionally, there were significant differences in DBLO of models with different transient sodium channel (Na_T) kinetics. Although these factors were not strong enough to produce high DBLO independently, clubbing them together produced models with high DBLO. We show that predictions of ion channel conductance differ significantly between models with high DBLO and models which match other electrophysiological properties but not DBLO levels. Such details can be biologically and medically important, such as during seizures (Quraishi et al., 2019). Furthermore, high DBLO plays a nuanced role in certain signature properties of neuronal firing, such as firing bistability due to persistent sodium channels.

Results

CA1 pyramidal neurons exhibit high DBLO

To first characterize DBLO in CA1 pyramidal neurons, we recorded membrane potential from mouse hippocampal CA1 pyramidal neurons (N=13) while injecting a series of step currents for 500 ms. Fig 1A and Fig 1B show representative recordings from the soma of a neuron when 150 pA and 300 pA respectively were injected into the soma. We calculated the DBLO of these recordings which is denoted by the arrows between the horizontal dashed and solid line in Fig 1A and Fig1B. The Depolarization Baseline (DBL) is defined as the mean of the minimum membrane potential between two consecutive spikes, and the DBLO is defined as the difference between DBL and the resting membrane potential (E_{rest}) of the neuron. At 150 pA, the mean DBLO at 150 pA current injection across all the 13 neurons was 20 ± 4 mV (range of 12.7 mV to 29.5 mV). The 10 to 90 percentile range of DBLO at 150pA current injection was 15.4mV to 25.9mV. For our study we chose this as our convention for labeling a DBLO as low (<10 mV), moderate (10 to 15.4 mV) or high (15.4 to 25.9mV).

The DBLO of neurons increased with the amount of current injected (Fig 1C). Although Ohm's law ($\Delta V = I*R$) predicts this, it could not explain the absence of correlation between the input resistance (Rin) and the DBLO (Fig 1D, Spearman's correlation coefficient r=0.21, p-value=0.49). On the other hand, the neuron's total capacitance was found to be moderately inversely correlated with DBLO (Fig 1E, Spearman's correlation coefficient r=-0.59, p-value=0.035).

Thus in this first section we experimentally characterized DBLO from mouse CA1 pyramidal neurons.

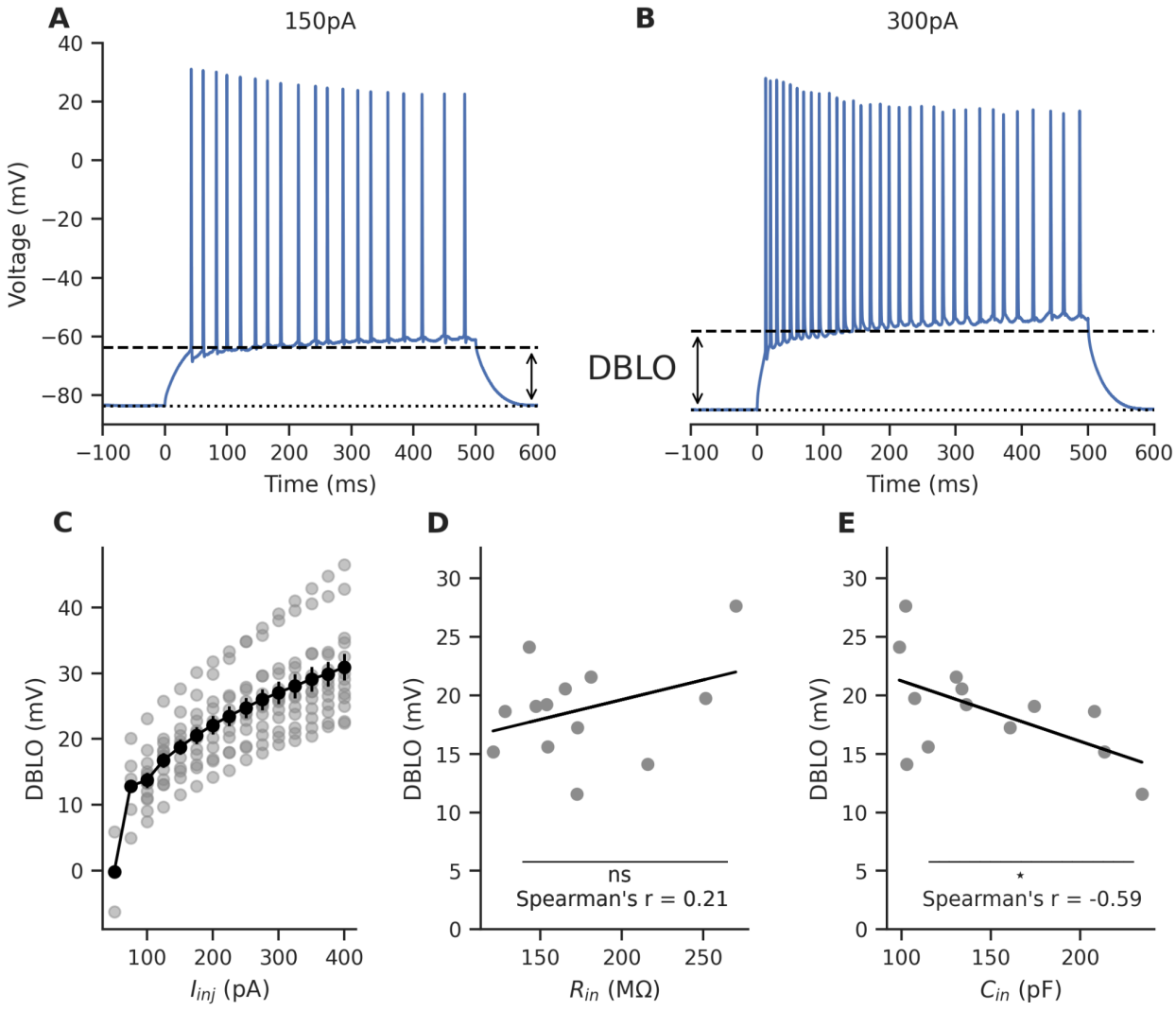

Fig 1. Experimentally observed DBL features. A, Representative whole cell recording from a mouse CA1 pyramidal neuron showing a DBLO of 19.7 mV. 150pA current was injected into the soma of the neuron for 0.5 s starting at t=0 s. The horizontal dashed and solid lines represent the Depolarization Baseline (DBL) and E_{rest} of the neuron respectively. The potential difference between these two represents the DBLO. **B,** same as A but for 300 pA current injection. The DBLO here is 26.8 mV. **C,** The DBLO increases with the amplitude of injected current. Data from 13 recorded neurons are shown in gray. The black dots represent the mean DBLO at each injected current level. The error bars represent 1 standard error of mean (sem). **D,** DBLO shows non-significant correlation (Spearman's correlation coefficient r=0.13, p-value=0.68) with the input resistance (R_{in}) of the neuron. **E,** DBLO shows moderate negative correlation (spearman's correlation coefficient r=0.13, p-value=0.039) with the total cell capacitance (C_{in}) of the neuron.

Numerous conductance-based models of CA1 pyramidal neurons have low DBLO.

To examine how DBLO has been addressed in the simulation literature, we looked at some state-of-the-art CA1 pyramidal neuron conductance-based models with detailed morphology. We first calculated the DBLO in a set of pyramidal neuron models from ModelDB (McDougal et al., 2017) and the Allen Cell Types Database (http://celltypes.brain-map.org/). The original models were implemented in the NEURON simulator (Carnevale & Hines, 2006), hence we used NEURON for these calculations. Since these models were made with information from cells of different animals, and brain regions, they may show differences in intrinsic properties like input resistance and resting membrane potential. To rectify the differences in intrinsic properties of each model, we injected a current that produces 19 spikes in 500ms. This also avoided any effects that may have arisen from different firing rates and excitabilities of the models.

Source	Original DBLO	Correction	Final DBLO
Migliore et al., 2018	1 mV	Em reduced by 50 mV	16 mV
Turi et al., 2019	4.7 mV	Em reduced by 35 mV	13 mV
Tomko et al.,	14 mV	NA	NA
Gouwens et al., 2018	21 mV	NA	NA

Table 1: Selected pyramidal neuronal models and their DBLO levels.

The model of rat CA1 pyramidal neuron from (R. Migliore et al., 2018) showed a DBLO of only 1 mV (Fig 2A). Since the model did not correct for the experimental recordings for liquid junction potential (LJP), we compensated for the LJP in the models by decreasing the leak reversal potential (Em) of the model such that the resulting E_{rest} of the model was 15 mV lower than the E_rest of the original model. As mentioned above, we tested using a current that resulted in 19 spikes in 500 ms. We saw that there was an improvement in DBLO to ~16 mV (Fig 2B).

The rat CA1 pyramidal neuron model from (Turi et al., 2019), after adjusting for the number of spikes, also showed a low DBLO of 4.7 mV (Fig 2C) and this value was again increased to 13 mV after compensating for LJP (Fig 2D).

The rat CA1 pyramidal neuron model from (Tomko et al., 2021) showed moderate DBLO of 14 mV even in the absence of LJP correction (Fig2E). This is one of the few conductance based models of CA1 pyramidal models in our test set which showed DBLO that was just within the experimental range.

One of the rat cortical pyramidal neuron models from (Gouwens et al., 2018) showed a high DBLO of 21 mV. This study corrected their data for LJP. Although this model has a high

DBLO and other electrophysiological properties well within experimental range (Gouwens et al., 2018), the morphology and kinetics of ion channels used to build these models were taken from cortical pyramidal neurons instead of CA1 pyramidal neurons. The DBLO in the various models in Fig 2 are summarized in Table 1.

Thus this survey of models showed that DBLO can exist in Hodgkin-Huxley (HH) type conductance based models, and LJP correction increases DBLO. We next looked at LJP and its effect on high DBLO in further detail.

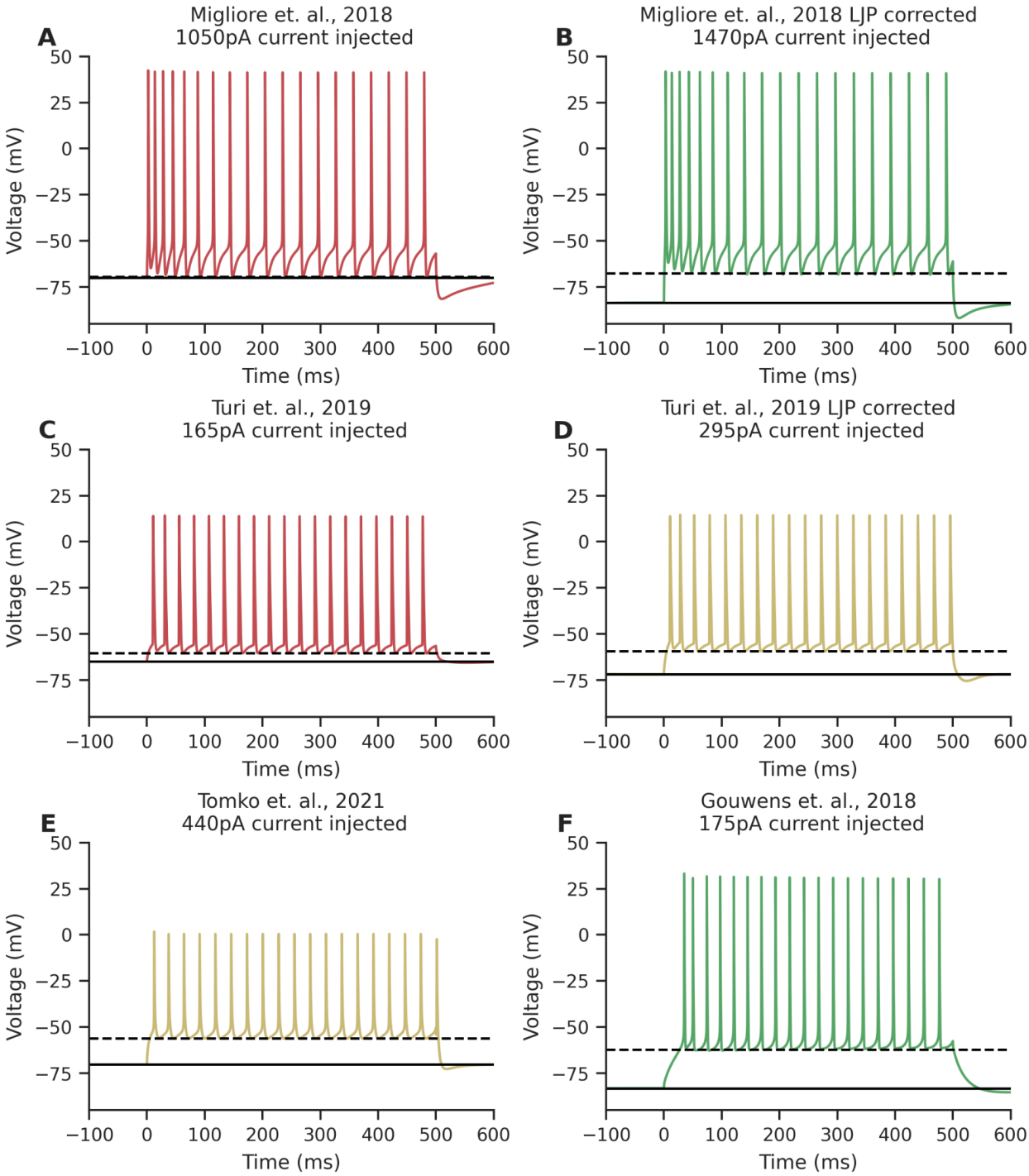

Fig 2. DBLO in a few state-of-art pyramidal neuron models. The injected current was chosen so as to get 19 spikes in 500 ms to match the representative experimental recording shown in Fig 1A. For representational purposes, models with low DBLO of <10 mV are colored red, models with moderate DBLO of 10 mV to 15.4 mV are colored yellow and models with high DBLO of >15.4 mV are colored green. **A,** Rat CA1 pyramidal neuron model from Migliore et al.,

2018 showing a low DBLO of 1 mV. **B,** A modified Migliore et al., 2018 model which accounts for LJP. Note the high DBLO of 16 mV. **C,** Rat CA1 pyramidal neuron model from Turi et al., 2019 with a DBLO of 4.7 mV. **D,** A modified Turi et al., 2019 model which accounts for LJP. Note the high DBLO of 13 mV. **E,** Rat CA1 pyramidal neuron model from Tomko et al., 2021 showing moderate DBLO of 14 mV. **F,** Rat cortical pyramidal neuron model from Gouwens et al., 2018 showing high DBLO of 21 mV

Liquid Junction Potential correction of experimental data is necessary for building models with high DBLO

We illustrate that the experimental recording needs to be corrected for Liquid Junction Potential (LJP) before using this data for modeling. Fig3A demonstrates the origin of LJP. LJP arises due to ion concentration differences between the intracellular and external buffer solutions used in experiments. See (Neher, 1992; Zielen, 1963) for details. The typical values of LJP can be anywhere between 0 mV and 20 mV depending on the solutions used. Some studies correct for this offset when they report membrane potentials, some studies do not but report the LJP offset values, while some studies ignore this phenomenon.

We first calculated LJP (15mV) from the buffers we have used in the pipette and external bath (Materials and Methods) and subtracted the LJP from the raw voltage traces to get the corrected traces. Fig 3B replicates Fig 1B with and without LJP offset correction, at 300 pA current injection. To understand how the Na_T channels might behave under the two scenarios, we computed the temporal evolution of its activation and inactivation variables under these two conditions. We used Na_T kinetics from (Royeck et al., 2008)(Fig 3C) and equations 8 & 13 which describe this temporal evolution for this purpose. The inactivation gate did not recover after the first spike in the case of the trace where LJP was not corrected (Fig 3D left). However, for the LJP corrected trace, the inactivation gate recovered to higher levels (Fig 3D right). This was because when LJP is not corrected, the DBL is at around -40 mV (green dashed line in Fig 3B and Fig 3C). At this high potential, the steady state of the inactivation variable is almost 0 (Fig 3C), thus all the Na ion channels would get inactivated. If the LJP is corrected, the DBL is at around -60 mV where the inactivation gate does not fully inactivate (red dashed line in Fig 3B and Fig 3C). Hence without LJP correction, the models will not lead to action potentials (AP) at such high DBL.

Having explored the role of LJP as a key criterion to get high DBLO, we next examined how passive and morphological properties of a neuron might affect DBLO. For the remainder of results, only LJP corrected data is used.

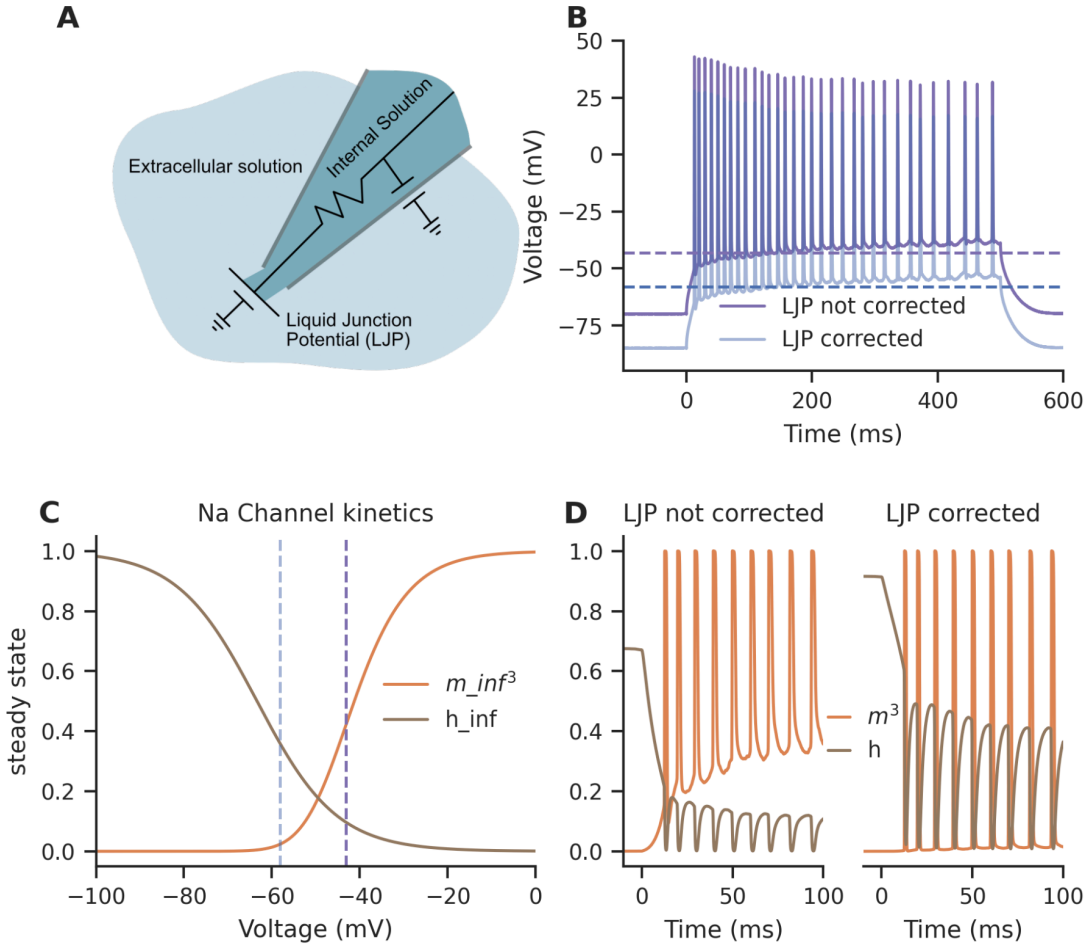

Fig 3. Not accounting for LJP leads to Na channel inactivation at high DBL. A: Illustration showing the source of LJP. LJP emerges when liquids of different electrolytes come into contact. **B:** Representative experimental recording at 300 pA current injection in a CA1 pyramidal neuron where LJP is accounted for (light blue) and not accounted for (dark blue). Dashed lines indicate respective DBL. **C:** Steady state activation and inactivation curves of Na_T kinetics. Dark blue vertical dashed line represents the DBL when 300 pA current is injected into a CA1 pyramidal neuron and LJP is not accounted for. Light blue vertical dashed line represents the DBL when 300 pA current is injected into a CA1 pyramidal neuron and LJP is accounted for. **D:** The experimental recording shown in B was used to calculate the opening probabilities of the Na_T gates m and h. In the case where LJP was not corrected, the inactivation gate did not recover after the first AP and further APs were not possible (left panel). In the case where LJP was corrected, the inactivation gate partially recovered after the first AP and further APs were possible (right panel).

Localizing ion channels in Axon Initial Segment results in high DBLO but low spike amplitudes

In most pyramidal neurons, the Axon Initial Segment (AIS) is the initiation center of APs and expresses major ion channels required for action potential initiation (Colbert & Johnston, 1996; Kole et al., 2008). Since experimental recordings are usually taken from the soma, we hypothesized that due to the RC(Resistor–Capacitor) filtering property of the membrane stretch between AIS and soma, the APs generated at AIS will experience low pass filtering. This may result in the filtering out of the trough which is a high frequency part of the AP shape, thus leading to increased DBLO.

To test this, we built two compartment models with passive soma, and Na_T and K_DR in the AIS. An illustration of the morphology and the hypothesis is shown in Fig 4A. The passive parameters, maximal conductance of Na_T (Na_T_Gbar) and maximal conductance of K_DR (K_DR_Gbar) (base K_DR) were kept as free parameters when generating these models. The models were considered valid only if their passive properties were within experimental range and firing frequency was within the 10-90th percentile range of experimental data (see materials and methods for detail). We observed that indeed the DBLO increased with an increase in the axial resistance (RA) which is a proxy of the electrotonic distance between the AIS and DBLO (Fig 4B). However, apart from the DBLO increase, we also saw that the spike height decreased to non-physiological levels as RA increased (Fig 4C). 150 pA responses of two representative models that showed high DBLO and low DBLO are shown in Fig 5D with the high DBLO model showing extremely low and non-physiological AP amplitude.

Thus, the initiation of APs in AIS alone cannot reconcile high DBLO with observed spike amplitudes. We therefore did not separate AIS and soma in subsequent results and analysis. We next looked at whether dendritic morphology can affect DBLO.

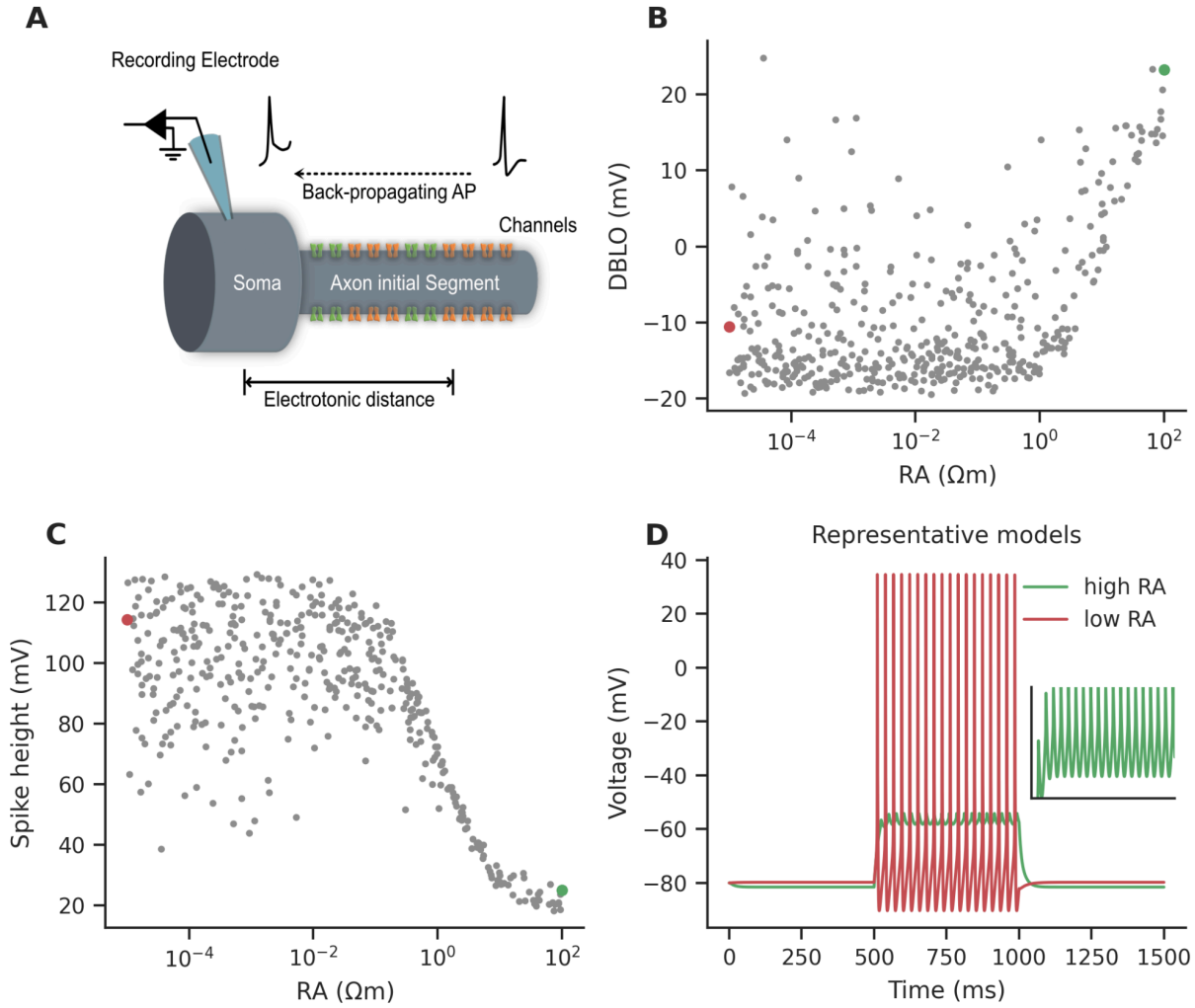

Fig 4. High DBLO is not due to AP initiation in AIS. A: Morphology and ion channel distribution. The ion channels were inserted into the AIS section and soma was kept completely passive. **B:** DBLO was positively correlated with the RA (Pearson's r = 0.60, p-value=5.35e-46). **C:** The spike height decreased to non-physiological levels when RA was increased (Pearson's r = -0.55, p-value = 8.77e-38). **D:** Two extreme models with the highest RA (green) and the lowest RA (red). Since the spike height of the highest RA model is too low, its APs are not visible. The APs are visible in the inset which shows the zoomed trace. The inset features an x-axis spanning 500ms to 1000ms while the y-axis extends from -59.2 mV to -54.2 mV. The highest RA and lowest RA models are indicated by a green dot and red dot respectively in panel B and C.

Multicompartment models with physiological frequency responses produce higher DBLO than single compartment models

(Hendrickson et al., 2011) showed that the afterhyperpolarization (AHP) was shallower in models with higher dendritic resistance. Higher dendritic resistance meant the dendritic compartments charged to a higher level during AP depolarization and subsequently, during somatic repolarization, dendritic axial currents fed into the soma causing shallower AHP. Thus, we hypothesized that a similar mechanism may affect DBLO.

We first developed three families of subthreshold models - single compartment models (1comp) that match the passive features of the recorded CA1 pyramidal neurons, passive models (pas) with ball and stick morphology that also match the passive features of the recorded CA1 pyramidal neurons, and full impedance (imp) models that match both the passive features and the subthreshold impedance amplitude of the recorded CA1 pyramidal neurons (Fig 5A). For passive features, we fitted the -25pA response of the models to that of the experimentally recorded neuron's. This captured the experimental passive properties like E_{rest}, R_{in}, C_{in}, and tau. For impedance amplitude, we injected a chirp current with a subthreshold amplitude of 30 pA which spanned 0 Hz to 500 Hz in 13 s (Material and methods). We recorded the voltage response and calculated the subthreshold impedance amplitudes from these recordings (Fig 5B). To build imp models, we fitted the impedance amplitude of the ball and stick model to that of the experimentally recorded neuron's. This procedure captured the neuron's morphological characteristics and its contribution to the voltages at soma at various frequencies. This procedure generates a single 1compt model, a single imp model and ten pas model for each of the 13 neurons.

We then made model triplets for each neuron by picking the corresponding 1compt model, imp model and one of the ten pas models. We then incorporated Na_T and K_DR into these models such that within each triplet, the maximal conductance (Gbar) of the three ion channels was the same. A total of N=4248 active models were built in this manner.

We observed that DBLO in imp models was significantly higher than in pas or 1compt models (Fig 6D). In addition, DBLO in pas models was also significantly higher than in 1compt models (mean DBLO in 1compt = -4.3 mV, pas = -3.7 mV, imp=-1.9 mV, repeated measures ANOVA F statistic=34.21, p-value=0. paired test 1compt vs imp p-value=0, 1compt vs pas p-value=0, pas vs imp p-value=0).

Very few (2 each) of the 1compt and pas models in our parameter sweep exhibited even moderate DBLO. Imp models, on the other hand, yielded 64 models with moderate DBLO. We compared the models within triplets, and found that on average the imp models had 2.4 mV higher DBLO than the 1compt model, while the biggest difference was 7.15 mV.

To remove the effects of different firing rates in the models, we also plotted the DBLO as a function of the number of spikes in response to 150 pA within 500ms (Fig 5E). Here too, the imp models showed higher DBLO than pas or 1compt models.

These calculations showed that the morphology contributes significantly to the DBLO. We next moved to investigate the role of ion channel kinetics on DBLO.

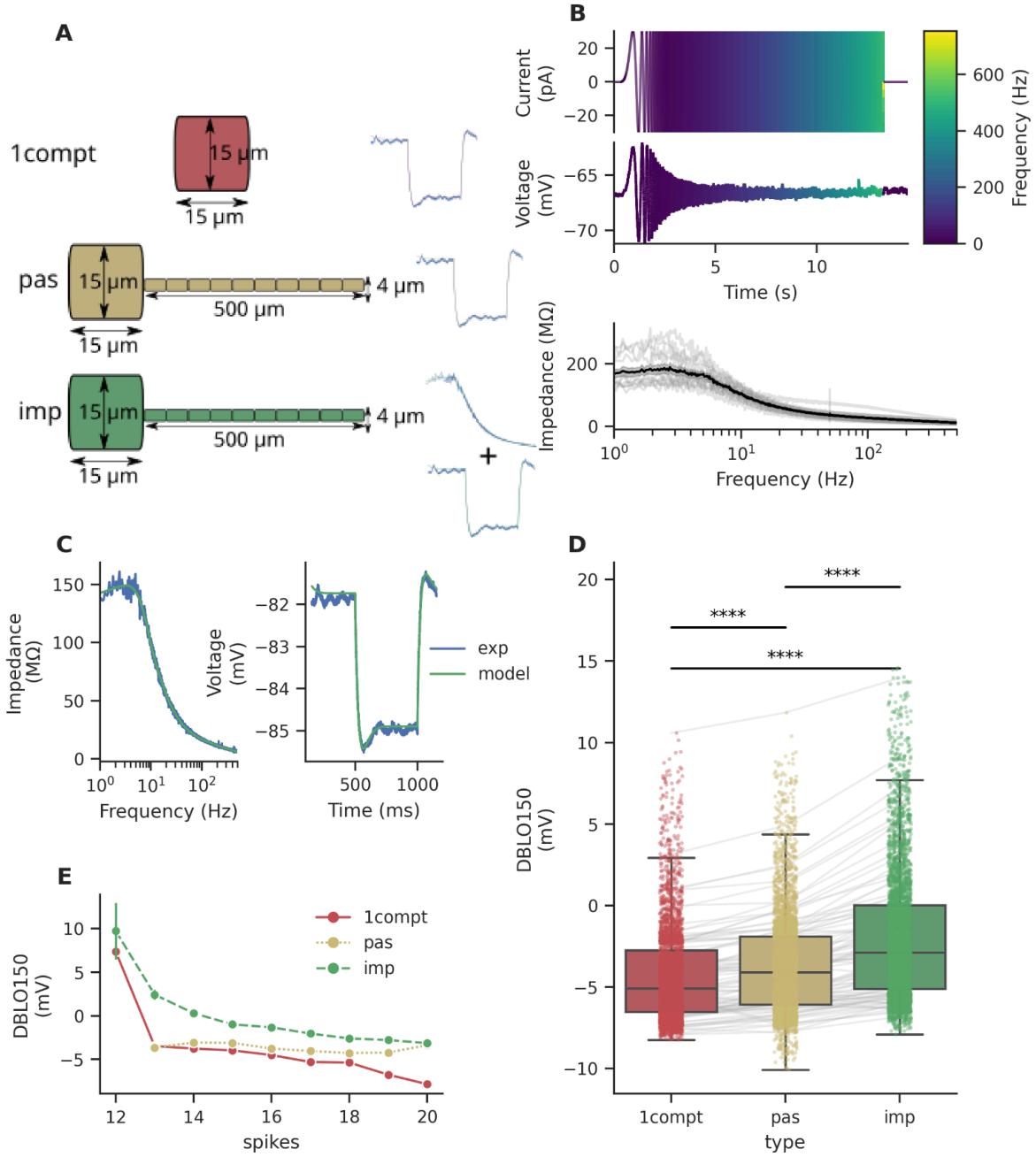

Fig 5. Morphology affects DBLO. A: The morphologies used for generating Imp, pas and 1compt models, and the experimental data to which they were fitted. **B:** Chirp response and impedance. Upper panel shows a representative current injected. Middle shows the corresponding voltage recorded from a neuron. The color represents the sinusoidal frequency of

the injected current. In the lower panel the black curve shows the mean impedance amplitude calculated from the voltage response and the current injected from all the 13 recorded neurons. Grey lines represent impedance amplitude profiles of individual neurons. **C**: Passive fits for representative imp model and its source neuron. Left: Impedance amplitude profile. Right: -25 pA response. **D**: DBLO comparison for all sampled models The Imp models had higher average DBLO than pas and 1compt models (see main text for details and stats). **E**: Mean DBLO comparison for population of models separated by number of spikes when 150pA current is injected for 500 ms. As before, imp models have higher average DBLO.

High K_DR reversal potential does not explain high DBLO

Next we wanted to see if K^+ channels have any effect on DBLO. We first checked if the reversal potential of K_DR had any effect on DBLO. We hypothesized that a more depolarized reversal potential (Erev) would result in low driving force of the K_DR channel and hence would lead to high DBLO. To check this, we did a stochastic parameter search with Na_T_Gbar, K_DR_Gbar and K_DR Erev as free parameters. We indeed found that high K_DR Erev resulted in high DBLO (Fig 6A). However, high DBLO at 150 pA was achieved only when the K_DR Erev was at non-physiological levels of above -70 mV. Further, we expect that DBLO should increase with higher current as shown above (Fig 1C) and in an experimental representative neuron recording at 150 pA and 300 pA (FIg 6A). However, the models with high K_DR reversal potentials did not show this current-dependent increase in DBLO. The model with lowest DBLO is shown in Fig 6B while the model with highest DBLO is shown in Fig 6C. These two models show minimal increase in DBLO when injected current is increased, which is inconsistent with the recordings.

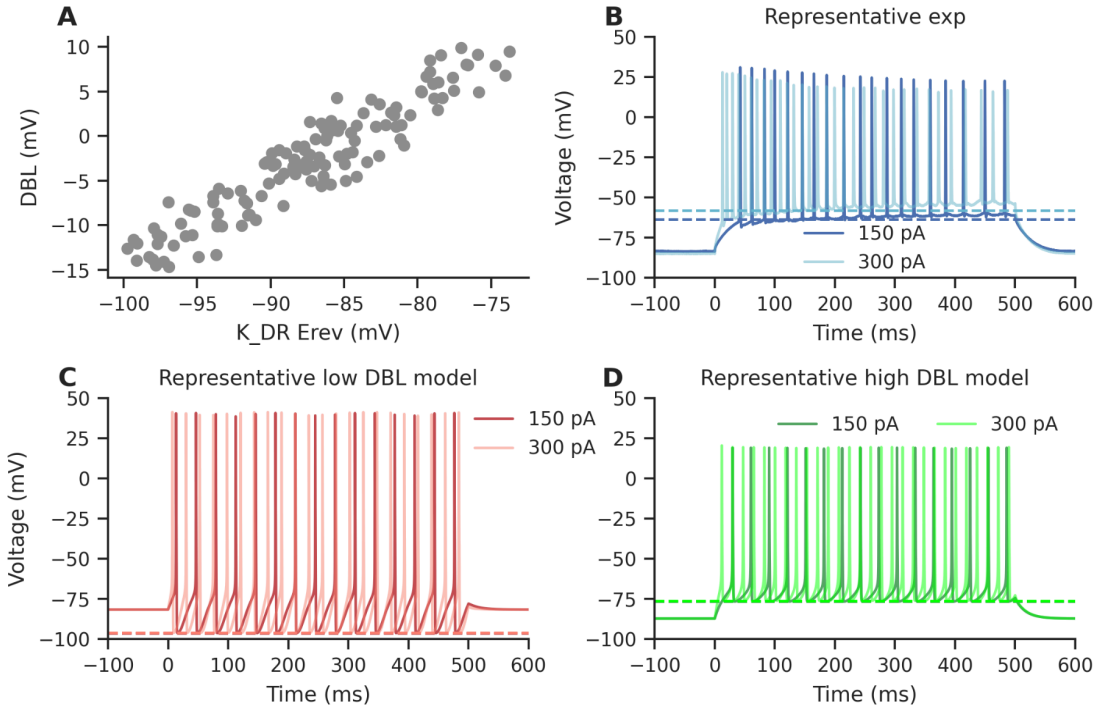

Fig 6. Unphysiologically high Erev of K^+ channel gives rise to high DBLO. A: DBL increases with higher Erev for K_DR, but requires unphysiologically high Erev to obtain high DBLO (pearson's r = 0.94, p-value = 7.45e-60). **B:** Representative experimental recording showing that DBLO increases with injection current. **C**: Low DBLO model which does not show current-dependent increase in DBLO. **D:** High DBLO model using shifted Erev for KDR, which does not show current-dependent increase in DBLO.

Fast potassium channel deactivation kinetics result in higher DBLO than slow kinetics

We hypothesized that if the deactivation of K_DR is fast, K_DR would quickly close during the repolarization phase of an AP. This would result in faster AP termination and hence high DBLO. Thus, to test this hypothesis and to explore the role of potassium channel kinetics in the high DBLO phenomenon, we constructed a thousand single compartment models which had their passive features and firing frequency within the experimental range (Materials and Methods). Model morphology and the equivalent electrical circuit are given in Fig 7A. In constructing these models, Em, CM, RM, Na_T_Gbar and K_DR_Gbar, and K_DR kinetics were kept as free parameters. Figure 7B illustrates the parameters that define the tau curve of the K_DR channel.

Other than n_E which is the parameter that controls the slope of the time constant at low potentials, there was no correlation between DBLO and those parameters (Fig 7C-O) in the models. For n_E we observed a significant but weak negative correlation with DBLO (Fig 7M). Low values of n_E correspond to low tau (fast deactivation kinetics) at low voltages as evident in Fig 7O where a strong correlation between DBLO and tau at -65mV in models can be seen. To illustrate the point, we compare 150 pA current injection traces from two representative models in Fig7P. The model shown in green has a DBLO of 7.8mV while the model shown in red has a DBLO of -21.1mV. The parameters associated with these models are indicated in Fig7B-O by green and red markings respectively. Notably, the tau at -65mV of the model with lower DBLO is indeed higher than that of model with higher DBLO reinforcing our hypothesis.

The Pearson's correlation coefficient r for the parameters varied vs DBLO are listed in table 2.

Parameter	Pearson's R	p value
K_DR_Gbar	-0.26	5.08e-12
Na_T_Gbar	-0.17	1.29e-5
n_A	0.05	1.72e-01
n_B	0.17	6.21e-06
n_C	0.05	2.39e-01
n_D	-0.14	4.24e-04
n_E	-0.37	2.68e-23
n_F	0.07	7.02e-02
K_DR Tau at -65 mV	-0.48	3.25e-40

Table 2: Pearson's correlation coefficients of parameters varied for exploring K_DR kinetics that gives high DBLO.

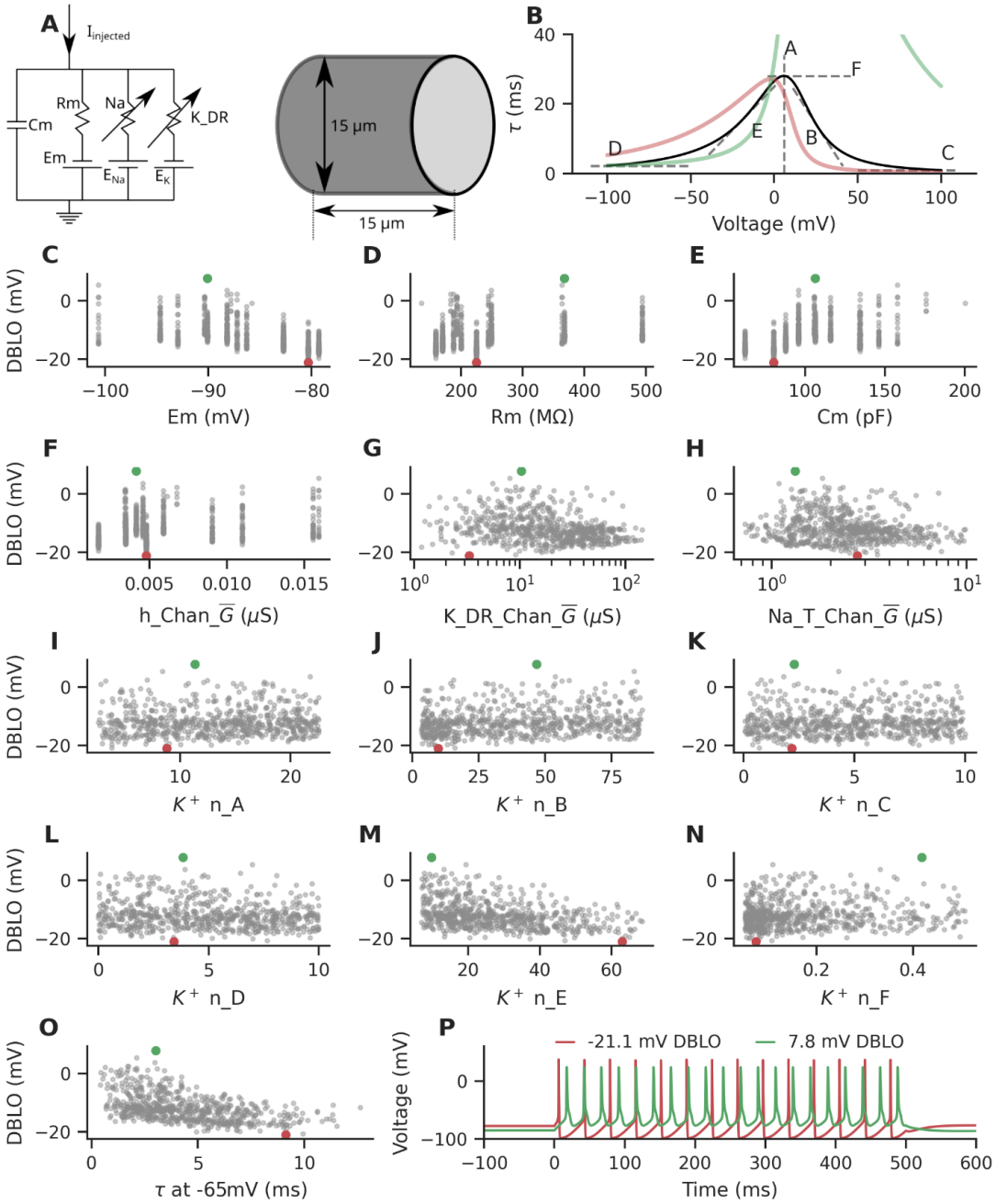

Fig 7. K_DR deactivation at hyperpolarized membrane potentials contributes significantly to DBLO. A: Equivalent circuit diagram of the model. A single compartment model with 15 µm length and 15 µm diameter was used. **B:** The parameterized K_DR kinetics. Parameter A controls the peak location, parameter B controls the slope of the curve at high potentials,

parameter C controls the minimum time constant at high potentials, parameter D controls the minimum time constant at low potentials, parameter E controls the slope of the curve at low potentials, and parameter F controls the peak height. Green and red curves are the K_DR kinetics of models presented in panel P. **C-N:** The DBLO in models plotted against parameter values. Green and red dots are the parameters associated with models presented in panel P. **O:** DBLO vs. time-constant tau at -65 mV of K_DR deactivation**.** A moderate negative correlation is seen between tau and DBLO, details in text and Table 2. Green and red dot is the tau at -65 mV of K_DR kinetics associated with models presented in panel P. **P:** Response to 150 pA of the model that expresses the lowest DBLO (colored in red) and of the model that expresses the highest DBLO (colored in green). The parameters corresponding to these models are shown as red and green dots respectively in panels B-O.

Na_T kinetics has significant impact on DBLO

To check whether Na_T kinetics might have any effect on DBLO, we made three types of active models, referred to as Gouwens, Royeck and Migliore, respectively. In all three types of models, we used the 1compt models generated previously and default slow K_DR kinetics. For Gouwens models, we incorporated Na_T kinetics from (Gouwens et al., 2018) which is in turn based on (Hay et al., 2011) with experimental kinetics from neocortical layer 5 pyramidal neurons of rats (Colbert & Pan, 2002). For Royeck models, Na_T steady state curve was taken from experimental data from mouse CA1 pyramidal neurons (Royeck et al., 2008). Since their study did not provide tau curves, we used tau curves from (Hay et al., 2011). This is the kinetics used in all the simulations up until now. For Migliore models we used Na_T kinetics used in (R. Migliore et al., 2018). This kinetics was further based on (M. Migliore et al., 1999) where the experimental kinetics from rat CA1 pyramidal neuron dendrites (Magee & Johnston, 1995) was slightly modified. The kinetics are shown in Fig8A. For each model group, we varied the Gbar of the Na_T and K_DR channel while picking one of the thirteen 1compt models at random. We tested 6500 model configuration per group and rejected models which did not have active properties within experimental range (see Materials and methods).

We saw that there was a significant difference in the median DBLO levels of the three groups of models (Fig 8B). Gouwens models had the largest mean DBLO and it was also the only group with a few (5) moderate DBLO models out of a total of 406 valid models (no models with high DBLO). Post-hoc Dunn test revealed that there was no significant difference between the Gouwens and Royeck group while the DBLO's were significantly different in the pairwise comparisons between Gouwens vs Migliore, and Migliore vs Royeck (statistical data in Fig 8 legend).

Up until now we saw that optimization of morphology, K_DR and Na_T kinetics independently can increase the DBLO significantly from when default values are used. Next we show that combining these factors give rise to high DBLO models. We also explore the implication of considering DBLO while building conductance based models.

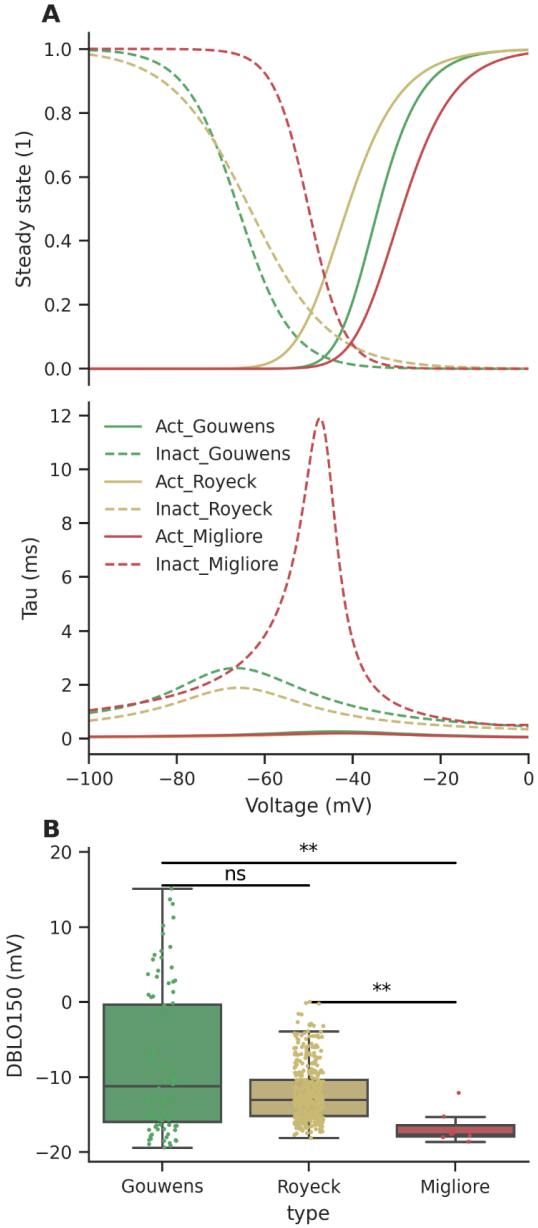

Fig 8. Effect of Na_T kinetics on DBLO. A: Na_T kinetics from three different sources - Gouwens et al., 2018, Royeck et al., 2008, and Migliore et, al., 2018. The upper panel shows the steady state curves of the activation (solid lines) and inactivation (dashed lines) gates. The lower panel shows the tau curves. **B:** DBLO was significantly different between models made using the three Na_T kinetics (Kruskal-Wallis H-test, statistic=13.4, p-value=0.0012). Na-T kinetics from Gouwens showed highest mean DBLO of -8.3 +- 9.4 mV, followed by Royeck, with

mean DBLO of -12.2 +-3.7 mV, and Migliore, with mean DBLO of -16.7mV +-2.3 mV. The differences in medians between Gouwens and Royeck models was not significant (Dunn's post-hoc test p-value = 0.3) while the Gouwens vs Migliore (Dunn's post-hoc test p-value = 0.001) and Migliore vs Royeck (Dunn's post-hoc test p-value = 0.0043) were significant after Bonferroni correction.

Models with DBLO have constrained conductance ranges

We showed above that multiple factors contribute to DBLO, mainly K_DR deactivation kinetics, and the subthreshold impedance profile of the neuron. Although these factors had a significant effect on DBLO, they could not separately account for high DBLO seen in our recordings. To check whether combining these factors would result in high DBLO models, we used the imp models generated previously, incorporated a fast deactivating K_DR channel and used Na_T kinetics from (Gouwens et al., 2018). A stochastic parameter search on Gbars of the Na_T and K_DR channels and these modifications gave us 19 models (out of 65000 combinations tested) that had high DBLO of more than 15.4mV. One such representative model is shown in Fig 9A.

To explore whether Na_T_Gbar and K_DR_Gbar show any dependence on DBLO levels, we plotted the ratio between the maximal conductances against DBLO in the models we built in the preceding paragraph. We saw that the ratio of maximal conductance levels was moderately correlated with DBLO (Fig 9B and Table 3) implying that models built without considering DBLO may give different quantitative predictions about the maximal conductance levels of ion channels as compared to models which were built while keeping DBLO as a feature. This correlation may be biologically significant as the Gbar ratio more than quadrupled in models with DBLO of 15mV compared to models with DBLO of -10mV (Fig 9B). To check if this was not an effect confounded by the different models having different excitabilities, we grouped the models by the number of spikes they produce when 150 pA current is injected for 500 ms. The positive correlation was maintained in all cases except for the 20-spike dataset (Fig 9B and Table 3).

Firing bistability may depend on interactions between Na_P and DBLO

To look for qualitative problems that might arise from not having DBLO as a feature while building models, we looked at firing bistability. We hypothesized that ion channels may play different roles in intrinsic firing bistability of high DBLO models and low DBLO models. To confirm this, we added Na_P channels at varying levels to active imp models generated for Fig 5, and the valid models generated above (see materials and methods for details). We then checked if the models showed firing bistability. We defined firing bistability in our case as the ability of a neuron to switch between tonic firing and silent mode when depolarizing and hyperpolarizing currents are injected respectively.

We found out that for imp models, only models with high DBLO showed firing bistability (Fig 9C left panel). Models with low DBLO either only fired during the depolarizing current injection window, or they were only silent during the hyperpolarizing current injection window (Fig 9C right panel). This implies that if one does not consider DBLO while building models, they might make the wrong prediction that Na_P cannot impart bistability to a neuron even if it might as seen in our case.

On the other hand, for the other set of models, firing bistability models were obtained both for low and high DBLO (data not shown). This illustrates that Na_P and high DBLO can

interact in distinct ways with other ion channels to generate firing bistability in a neuron type. Thus, ignoring DBLO as a criterion for neuronal model accuracy might lead to incorrect predictions about the role of ion channels in the neuron's function.

Number of spikes	Pearson's r	p-value
All models	0.47	1.87e-33
12	0.44	1.25e-02
13	0.45	1.22e-03
14	0.42	2.46e-03
15	0.44	6.73e-04
16	0.54	1.26e-06
17	0.54	4.74e-06
18	0.52	2.25e-04
19	0.39	4.91e-03
20	0.48	1.07e-01

Table 3: Pearson's r for comparison between DBLO and Gbars of Na_T and K_DR. The models were grouped by the number of spikes they produced when 150 pA current was injected for 500ms. Except for the model group that produced 20 spikes, all other groups showed significant positive correlation. P-values have been corrected for multiple comparisons using Bonferroni correction.

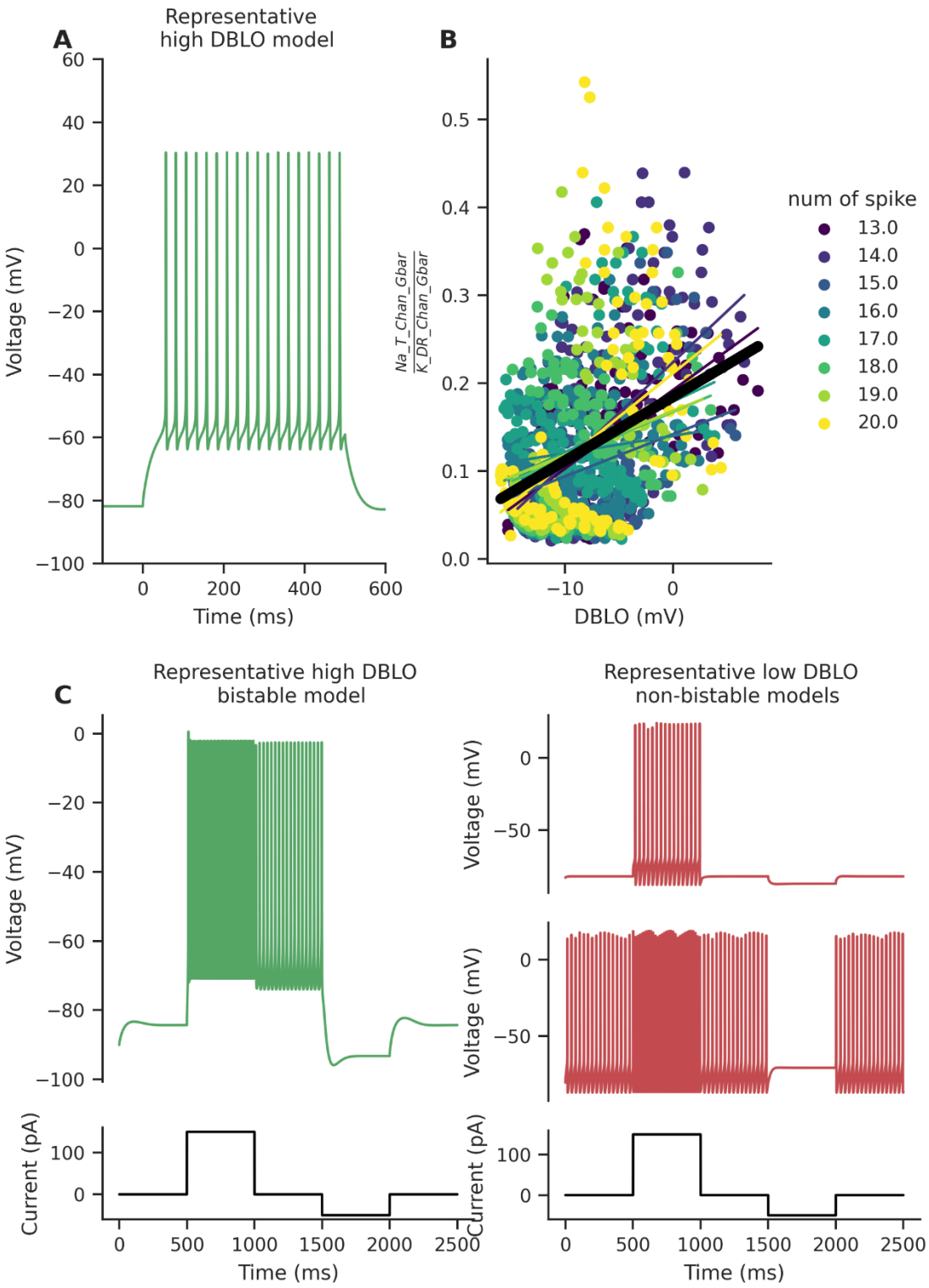
A
Representative
high DBLO model
Voltage (mV)
Time (ms)
B
Na_T_Chan_Gbar / K_DR_Chan_Gbar
DBLO (mV)
num of spike
13.0
14.0
15.0
16.0
17.0
18.0
19.0
20.0
C
Representative high DBLO
bistable model
Representative low DBLO
non-bistable models
Voltage (mV)
Current (pA)
Time (ms)

Fig9. Not considering high DBLO in models may lead to incorrect quantitative and qualitative predictions. A: Representative high DBLO model. The model used a ball and stick morphology which matched the subthreshold impedance amplitude profile of recorded neurons, had a fast K_DR kinetics and used Na kinetics from Gouwens et al., 2018. **B:** The ratio of maximal conductance of Na_T and K_DR increases significantly with DBLO in models (black line) indicating significant quantitative difference in the level of ion channel channels if DBLO are not considered while building models. The models were grouped based on the number of spikes they produce when 150 pA current is injected for 500 ms. A positive correlation is seen within most of these groups too (see table 3 for correlation coefficients and p-values). **C:** Na_P was incorporated into imp models at various levels and the models were checked for bistability. Bistability was seen only in models with high DBLO (left panel). Low DBLO models either only fired when 150 pA current was injected, or fired even when no current was injected (right panel).

Discussion

In this study we have used models and experiments to identify mechanisms that underlie a prominent feature of neuronal firing, Depolarization Baseline Offset (DBLO). We show that four factors majorly affect DBLO: LJP correction, the subthreshold impedance amplitude profile of models, fast deactivation kinetics of K_DR, and Na_T kinetics. Although high reversal potential of K_DR and low electrotonic coupling between soma and AIS give high DBLO, these modifications lead to non-physiological electrophysiological features and parameters. We use stochastic parameter search in conductance based models constrained by a range of physiological experiments, and also analyze the contributions of morphology. We finally show that the omission of DBLO as a constraint while building models may lead to incorrect estimates of levels of ion channels as well as incorrect predictions about the role of ion channels in several cellular functions. We took the example of firing bistability and showed that under certain conditions, Na_P imparts firing bistability to models with high DBLO but not to models with low DBLO. While in another it impart firing bistability to both high and low DBLO models.

Our analysis showed that although fast K_DR kinetics or physiologically matching impedance amplitude profiles were independently insufficient to produce high DBLO in models, their combined effects were enough to produce models with high DBLO within the experimental range. We thus conclude that high DBLO seen in experimental recording is likely due to a combination of different factors including fast KDR kinetics and morphology. It is also possible that another potassium channel with fast deactivation kinetics instead of K_DR is actually contributing to DBLO. A likely candidate could be the A-type potassium channel, which is known to have fast deactivation kinetics and which contributes a major portion of potassium currents in CA1 pyramidal neuron (Martina et al., 1998).

Tighter constraints for morphological simplification and passive properties

Subthreshold impedance amplitude profiles have been used previously to study the resonance property of neurons (Binini et al., 2021; Dhupia et al., 2015; Moradi Chameh et al., 2021; Narayanan & Johnston, 2007). Since a neuron's subthreshold resonance frequency is between 0-10 Hz (refs), these studies have used chirp stimuli that span 0 Hz to ~50 Hz. To the best of our knowledge, ours is the first study to use chirp stimuli that span 0 Hz to 500 Hz to measure subthreshold impedance amplitude profiles, and to use this to constrain multicompartment models. Rall et al., 1969 has previously shown that multicompartment neurons exhibit several time constants (Rall, 1969). The faster of these time constants affect the rapid depolarization and repolarization of soma during an AP as they are of the same timescale as an AP. Thus, the morphology of a neuron indirectly affects the shape and DBLO of a neuron, which we have captured by measuring the subthreshold impedance amplitude.

We find that this constraint over the subthreshold impedance amplitude works well even in our simplified models in which the dendritic section is a composite of all the neurites - proximal, apical, distal as well as axon. The caveat is that this simplification gives a much lower

electrotonic lengths (0.45 +-0.18) of the subthreshold impedance profile fitted models than experimentally determined median electrotonic lengths of 0.78 for CA1 pyramidal neuron apical dendrites (Turner & Schwartzkroin, 1983). This makes our reduced models currently unsuitable for studying distal synaptic inputs that impinge more than 0.45 electrotonic lengths away from the soma. Further constraints on the Postsynaptic potential (PSP) attenuation and impedance phase profile in our model would make these models useful to study synaptic integration, while keeping computational costs lower than for full scale models with detailed morphology.

We predict that correcting for DBLO may lead to at least three substantial alterations to the behavior of neural network models: E and I synaptic summation, firing bistability, and neuromodulator sensitivity. We address these in turn.

Implications for E/I balance and synaptic summation

Many real neural networks exhibit bursty activity in excitatory neurons, and modern models are able to capture these effects (Golomb et al., 2006; Roy & Narayanan, 2023; Tang et al., 2010). DBLO kicks in whenever the postsynaptic cell is firing briskly such as in bursts (Moore et al., 2009). (Bianchi et al., 2022) showed in their computational study that low DBLO models attenuated theta range synaptic activity while high DBLO models amplified gamma range synaptic activity. The presence of a high baseline can more than double the effective weight of a typical GABA-ergic synapse due to the increase in driving force. If we consider the LJP-corrected chloride reversal potential to be around -87 mV (Atallah & Scanziani, 2009; Barmashenko et al., 2011), and if DBLO raises the mean potential from around -82 mV to around -65 mV, we have a more than 200% increase in GABAR driving force. Thus the EI balance in models using neurons which lack DBLO, such as (Yu et al., 2014) may be impacted. This effect on inhibitory inputs is still more pronounced over brain development, since the GABA reversal potential starts out close to resting potential (Owens & Kriegstein, 2002; Peerboom & Wierenga, 2021). While very few network models consider early neuronal physiology, it is clear that the outcome of GABAergic inputs may flip from none, or even excitatory, to inhibitory when high activity results in DBLO. The effect of DBLO on synaptic summation of excitatory inputs is predicted to be smaller than that for inhibitory inputs, since the driving potential shift is only about DBLO/(E_{glu}-E_{rest}) or about 30%. Nevertheless, this too is a substantial effect during burst activity.

Implications to firing bistability

There are multiple specific proposed cellular computational functions that we predict will be impacted by DBLO. In Figure 8 we showed that a particular configuration of slow K_DR and Na_T kinetics did not allow Na_P to impart firing bistability to low DBLO models. Thus, this might make some low DBLO neurons resistant to Na_P induced firing bistability. Further analysis and more neuron-specific channel kinetic data will be required to show to what extent this constraint applies across different classes of neurons. In principle, the DBLO linkage to Na-P firing bistability has numerous implications to network function. For example, oscillations and epileptic activity have been linked to firing bistability (Fuentealba et al., 2005; Protachevicz

et al., 2019). Bistability has also been proposed to expand the dynamic repertoire of network models, especially attractors for memory (Lundqvist et al., 2010).

Implications for neuromodulation

Neuromodulators are ubiquitous control signals for causing networks to switch between states (Gutierrez & Marder, 2014; Marder et al., 2014). While they have been extensively analyzed in small CPGs (Golowasch, 2019; Williams et al., 2022), they also play a key role in setting network learning rates (Doya, 2002; Jepma et al., 2016; Rutledge et al., 2009). One of the key mechanisms by which neuromodulators affect neuronal activity is by modulating ion channels, which can be done by channel insertion or by phosphorylation (Nadim & Bucher, 2014). An accurate understanding of DBLO is relevant to this in two ways. First, many neuromodulated ion channels are potassium channels (Palacios-Filardo & Mellor, 2019). As discussed above for the case of GABA-ergic synapses, the current carried by K+ channels will be much larger during episodes of DBLO than at resting potential. This means that DBLO will amplify the effect of such neuromodulators selectively at times of high activity. Second, the current study shows that models which correctly express DBLO have significantly different channel distributions than uncorrected models (Fig 8A). Thus the substrate for neuromodulation itself (by way of density and distribution of K+ channels in particular) may be quite different. This has implications for studies which try to understand single-neuron activity changes arising from neuromodulation. Simply put, the correct DBLO model may respond differently to a neuromodulator than a model with similar firing activity but no DBLO.

Materials and methods

All code and experimental data is freely available on GitHub at: https://github.com/BhallaLab/DBLO_paper/tree/main

All simulations were carried out in MOOSE (Ray and Bhalla, 2008) except for Fig2 where NEURON was used to run the state-of-art models from ModelDB. These were performed on a 128 core AMD EPYC 7763 CPU machine with 1TB RAM and running Ubuntu Server 22.04.

For hypothesis testing, the Pingouin (Vallat, 2018) and Scipy (Virtanen et al., 2020) python libraries were used.

Four ion channel types were used in this study, namely transient sodium channel (Na_T), persistent sodium channel (Na_P), slow delayed rectifier channel (K_DR), and HCN channel (h). Below, we describe their kinetics in brief.

HCN channel kinetics was taken from (Hay et al., 2011) which in turn were based on the recordings of apical dendrites of cortical layer 5 pyramidal neurons of adult male Wistar rats (Kole et al., 2008). E_{rev} of HCN channels was kept at -40 mV. The equations that describe the kinetics are as follows:

$$I_h = m * \bar{g} * (v - E_{rev}) \quad \{1\}$$

$$\frac{dm}{dt} = \frac{m_{\inf} - m}{tau_m} \quad \{2\}$$

$$m_{\inf} = \frac{m_\alpha}{m_\alpha + m_\beta} \quad \{3\}$$

$$tau_m = \frac{1}{m_\alpha + m_\beta} \quad \{4\}$$

$$m_\alpha = 6.43 * \frac{v + 154.9}{e^{\frac{v+154.9}{11.9}} - 1} \quad \{5\}$$

$$m_\beta = 193 * e^{\frac{v}{33.1}} \quad \{6\}$$

Where v is in mV.

Three formulations of Na_T kinetics from different papers have been used in this study. Unless otherwise stated, the steady state or the inf curve of Na_T channel kinetics was taken from experimental recordings by Royeck et al., 2011 in the soma and AIS of mouse CA1 pyramidal neurons. Since Royeck et al., 2011 did not have data about the time constants, those were taken from Hay et al., 2011. We chose not to use the kinetics used in Migliore et al., 1999 as it was based on dendritic recordings from CA1 pyramidal neurons of adult Sprague-Dawley rats and the inactivation gate in the paper was modified. E_{rev} of Na_T channels was kept at 60 mV. The equations that describe the kinetics are as follows:

$$I_{Na_T} = m^3 * h * \bar{g} * (v - E_{rev}) \quad \{7\}$$

$$\frac{dm}{dt} = \frac{m_{\inf} - m}{tau_m} \quad \{8\}$$

$$m_{\inf} = \frac{1}{1 + e^{\frac{v+51}{-7.4}}} \quad \{9\}$$

$$tau_m = \frac{1}{m_\alpha + m_\beta} / Q_t \quad \{10\}$$

$$m_\alpha = 182 * \frac{-v-38}{e^{\frac{-v-38}{6}} - 1} \quad \{11\}$$

$$m_\beta = 124 * \frac{v+38}{e^{\frac{v+38}{6}} - 1} \quad \{12\}$$

$$\frac{dh}{dt} = \frac{h_{\inf} - h}{tau_h} \quad \{13\}$$

$$h_{\inf} = \frac{1}{1+e^{\frac{v+63}{9}}} \quad \{14\}$$

$$tau_h = \frac{1}{h_\alpha + h_\beta} / Q_t \quad \{15\}$$

$$h_\alpha = 15 * \frac{v+66}{e^{\frac{v+66}{6}} - 1} \quad \{16\}$$

$$h_\beta = 15 * \frac{-v-66}{e^{\frac{v+66}{6}} - 1} \quad \{17\}$$

$$Q_t = 2.3^{(T_{celsius} - 23)/10} \quad \{18\}$$

Where v is in mV.

The second Na_T kinetics formulation was from Migliore et al., 2018. This was only used in parts of Fig8. The third Na_T kinetics formulation was from Gouwens et al., 2018. This kinetics was used for parts of Fig8 and parts of Fig9.

The K_DR kinetics was taken from Migliore et al., 2018 but it was parameterized and written in a different form as described below:

$$I_{K_DR} = m * \overline{g} * (v - E_{rev}) \quad \{19\}$$

$$\frac{dm}{dt} = \frac{m_{\inf} - m}{tau_m} \quad \{20\}$$

$$m_{inf} = \frac{1}{1+e^{\frac{v-v_{1/2}}{-v_{slope}}}} \quad \{21\}$$

$$tau_m = \left(C + \frac{1 + \frac{yl}{\sqrt{(1+yl^2)}}}{2}\right) * \left(D + \frac{1 + \frac{yr}{\sqrt{(1+yr^2)}}}{2}\right) * F \quad \{22\}$$

$$yl = \frac{v-A}{-B} \quad \{23\}$$

$$yr = \frac{v-A}{E} \quad \{24\}$$

$$v_{1/2}, v_k, A, B, C, D, E, F = 0.013, 0.011, 1.26e^{-2}, 1.73e^{-2}, 0, 0, 3.43e^{-2}, 1.02e^{-1}$$

The parameterization was needed to explore the kinetics space that allows high DBLO. We tried different unimodal functions that can be used to parameterize the tau curves and found the eq{22} to be the most suitable. The A parameter controls the location of the peak of the tau curve, the F parameter controls the peak, the C parameter controls the tau at high Vm, the D parameter controls the tau at low Vm, the B parameter controls the slope of the tau at high Vm

and the E parameters controls the slope of the tau at high Vm (see Fig 7B for a visual representation). Its E_{rev} was kept at -100mV unless otherwise stated.

Finally, Na_P channel kinetics was also taken from Migliore et al., 2018. This ion channel was only used for parts of Fig9. Its E_{rev} was kept at 60mV.

State-of-art models

The CA1 pyramidal neuron model used in Migliore et al., 2018 was taken from modelDB accession number 244688. The Turi et al., CA1 pyramidal model was taken from modelDB accession number 246546. The Tomko et al., CA1 pyramidal model was taken from modelDB accession number 266901. The Gouwens et al., 2018 cortical pyramidal model was downloaded from http://celltypes.brain-map.org. The model ID was 486132712. For Migliore 2018 model and Turi 2018 model, where LJP was not corrected, we also made a version of the model where we modified the Em such that the resting membrane potential of the model came down by 15 mV. In each of the models, a 500 ms current pulse of different amplitudes was injected. The amplitude was chosen such that the number of spikes in each model during the 500 ms current injection matches the 150 pA representative experimental recording shown in Fig 1A.

Simulations of activation and inactivation gates

To record the opening and closing of Na_T gates in simulations, we took a representative 300pA experimental recording and used the Na_T kinetics equations {8-18} to numerically calculate the activation and inactivation gate opening probability values at each time point. We did the same calculation for a 300pA experimental recording that was not corrected for LJP.

The AIS model

The AIS models were generated with two compartments. The somatic compartment had dimensions of 15µm x 15µm while the AIS compartment had length of 30µm and diameter of 2µm. Em was fixed at -80mV. Na_T and K_DR channels were included only in the AIS compartment. Random values of the free parameters as listed in Table 4 were picked and several models were generated. Their R_{in}, C_{in}, E_{rest}, number of spikes in response to 500 ms of 0 pA current injection, number of spikes in response to 500 ms of 150 pA current injection, and average interspike interval (ISI) of APs in response to 500 ms of 150pA current injection were calculated. If these features were not within experimental range, the models were discarded. For subthreshold features, we considered the absolute experimental range while for suprathreshold features, we considered 10-90th percentile of experimental range. See table 5 subthreshold feature ranges and table 6 for suprathreshold feature ranges. Out of 5000 models tested, we got a total of 457 valid models. We also calculated each model's DBLO and spike height. The current injection and voltage recording in this case was done from the somatic compartment.

Free parameter (units)	symbol	Lower limit	Upper limit
Specific membrane resistance (Ωm^2)	RM	0.01	0.2
Specific axial resistance (Ωm)*	RA	1e-5	1e2
Specific membrane capacitance (F/m^2)	CM	0.086	0.124
AIS Na_T maximal conductance (μS)*	Na_T_Gbar	0.1	10
AIS K_DR maximal conductance (μS)*	K_DR_Gbar	1	1000

Table 4: Free parameters and their ranges for the unbiased stochastic search to test the AIS hypothesis. Parameters with * were not sampled uniformly but logarithmically with base 10.

Animal care

All animals used for the experiments were from BL6/J mice. Animals were raised with adequate water and food provided in the cage with a cage strength upto five. All animals underwent a 14 hr light and 10 hr dark cycle. Experimental animals were six to ten weeks old. Institute Animal Care and Resource Center(ACRC) staff ensured the health status, pathogen exposure and well being of all animals throughout the project timeline.

Ethics

All protocols performed were approved by the NCBS Institutional Animal Ethics Committee. Approval details: NCBS-IAE-2016/ 21 (ME); NCBS-IAE-2016/ 7(M);NCBS-IAE-2022/8 (R2M), Animal facility registration number: 109/GO/ReRcBiBt/S/99/CPCSEA.

Slice preparation

The slices were prepared from 6-10 weeks old (N=3) of BL6/J mice. Animals were decapitated after cervical dislocation, post anesthesia with Halothane. 400 um thick slices were made from the dissected hippocampus on a vibratome (LEICA VT-1200). The dissections and slicing were performed in cutting solution, artificial cerebro-spinal fluid (aCSF) with (in mM): NaCl-87, KCl-2.5, NaHCO3-25, NaH2PO4.H2O-1.25, Sucrose-75, MgCl2-7,CaCl2--0.5. Once sliced the slices were transferred to a holding aCSF with (in mM) : NaCl-124, KCl-2.7, NaHCO3-26, NaH2PO4.H2O-1.25, Glucose-10, MgCl2-1,CaCl2-2. Both solutions were saturated with 95%

O2 and 5% CO2. After an incubation time of 45 mins, slices were transferred to the recording chamber with holding-aCSF perfusion at 31+/-1 °C.

Electrophysiology

We used an infrared Differential Interference Contrast (DIC) microscope(Olympus BX51WI) with 40x (Olympus LUMPLFLN, 40XW) water immersion objectives to visualize the cells. The electrophysiology data was acquired using Axon™ Digidata® 1440B digitizer and MultiClamp 700B amplifier (Molecular devices, Axon instruments). We used 20 KHz sampling frequency and a 0-10KHz Bessel bandpass filter for the acquisition of electrical signals. We performed whole cell patch recordings from CA1 pyramidal cells. The electrodes were made from thick walled borosilicate glass capillaries (OD-1.5mm, ID-0.86mm). We used a P-1000 pipette puller from Sutter Instruments, Novato, CA with a box filament. Electrodes were filled with (mM): K-Gluconate-130, NaCl-5, HEPES-10, Na4-EGTA-1, MgCl2-2, Mg-ATP-2, Na-GTP-0.5, Phosphocreatine- 10, pH adjusted to 7.3 and osmolarity adjusted to ~290 mOsm. Liquid junction potential was 15mV. It was calculated according to the stationary Nernst–Planck equation (Marino et al., 2014) using LJPcalc software (https://swharden.com/LJPcalc). Experimentally recorded voltages were corrected for LJP except when stated otherwise.

Cells were picked for analysis based on the stability of series resistance (input resistance change less than 20% between the start of the recording and the end of recording), and resting membrane potential (a shift of less than 2.5 mV between the start of the recording and the end of recording). Out of 14 cells that we recorded from, 13 cells passed the criterion.

Recording chirp responses from mouse CA1 pyramidal neurons

To record the subthreshold impedance amplitude of neurons, we injected a chirp stimulus with time varying frequency into the neuron and recorded its voltage response using a whole cell clamp setup (as described above). The chirp stimulus was generated using the function:

$$I_{inj} = I_A * sin(2 * pi * t^3) \quad \{25\}$$

Where I_A is 30pA

We injected this current for 13s. During this time the frequency went from 0 Hz to 500 Hz in a quadratic manner (Fig{6b}).

The impedance amplitude was then calculated as:

$$Imp = \left| \frac{fft(v)}{fft(I_{inj})} \right| \quad \{26\}$$

Subthreshold feature calculation

To measure the subthreshold features of both experimentally recorded neurons and models, a 500 ms pulse of -25 pA current amplitude was injected. The first 100 ms of the -25 pA current injection response was fitted to the following equation:

$$V = E_{rest} - R_1 * 25e^{12} * (1 - e^{-t/tau1}) - R_2 * 25e^{12} * (1 - e^{-t/tau2}) \quad \{27\}$$

The R_{in} (input resistance) was defined as the higher of the two parameters R_1 and R_2. The higher of the two parameters tau1 and tau2 was taken as tau_m (membrane time constant) and C_{in} (input capacitance) was calculated as tau_m/R_{in}.

The E_{rest} was calculated as the median membrane potential at 0 pA current injection of 500 ms in both models and experimental recordings.

The steady state voltage response (V_ss) at -25 pA current injection was calculated as the median membrane potential of the last 100 ms of the voltage response to the 500ms pulse.

The subthreshold features along with their median and experimental range is given in table 5.

Feature (unit)	symbol	median	Minimum	Maximum
Input resistance (MΩ)	R_{in}	155	117	261
Input capacitance (pF)	C_{in}	95	47	171
Resting membrane potential (mV)	E_{rest}	-83.3	-87.3	-78.8
Charging time constant (ms)	tau	18.7	6.5	26.9
Sag ratio (1)	sag_rat	0.23	-0.013	0.64

Table 5: Subthreshold features of experimentally recorded neurons.

Suprathreshold electrophysiological feature calculation

For calculating the suprathreshold electrophysiological features, we used a combination of BlueBrain's eFEL library (Ranjan et al., 2024) and custom code. The summary of these features for the experimentally recorded neurons is given in Table 6.

The avg ISI feature was needed when generating valid active models to avoid models that had a valid number of APs but exhibited irregular firing.

Feature (unit)	symbol	median	10th percentile	90th percentile
Average firing rate during a 500pA pulse of 0pA amplitude (1)	freq_0	0	0	0

Average firing rate during a 500pA pulse of 150pA amplitude (1)	freq_150	36	24	42
Average ISI during a 500pA pulse of 150pA amplitude (ms)	ISIavg_150	27	23.6	39.2
DBLO during a 500pA pulse of 150pA amplitude (mV)	DBLO_150	20.3	15.4	25.9
Amplitude of first AP during a 500pA pulse of 150pA amplitude (mV)	AP1_amp_150	98	78	101

Table 6: Suprathreshold features of experimentally recorded neurons.

Generating valid subthreshold single compartment models

To generate valid subthreshold single compartment models (termed 1compt mdoels), we used a single cylindrical compartment of diameter of 15μm and length of 15μm. We employed a custom algorithm (included on the GitHub repository for this paper) to generate valid models. The algorithm combines stochastic search and gradient descent to generate a single valid subthreshold model corresponding to each of the recorded CA1 pyramidal neurons. In the first step of stochastic search, we picked uniformly distributed random values of 3 free parameters namely - membrane resistance of the compartment (sm_RM), total capacitance of the compartment (sm_CM), and maximal conductance of the HCN channel (h_Chan_Gbar). Em was then calculated to give the same E_{rest} as the corresponding neuron's E_{rest}. Table 7 gives the range from which these values were picked. We generated 1000 such random models and recorded their response to 500ms of -25 pA current injection (V_{-25}). Then, for each of the experimentally recorded cells, we found the 10 models out of the 1000 that had the least root mean square error (rms) between the V_{-25} of the model and the experimentally recorded cell. Thus, we got 10 best models corresponding to each neuron. We then employed scipy's curve_fit function to fit these 10 best models to the corresponding neuron's V_{-25}. Finally we picked the best out of the 10 to get a single valid passive single compartment model for each of the 13 experimentally recorded neurons for a total of 13 models.

Free parameter (units)	symbol	Lower limit	Upper limit
Specific perisomatic membrane resistance (Ωm^2)	sm_RM	0.07	0.4
Specific perisomatic membrane capacitance (F/m^2)	sm_CM	0.057	0.3
Perisomatic HCN channel maximal conductance (μS)	h_Chan_Gbar	0.001	0.07

Table 7: Free parameters and their ranges for the unbiased stochastic search to generate valid subthreshold 1compt models.

Generating valid subthreshold features fitted ball and stick models

To generate valid passive ball and stick models (termed pas models), we used a morphology with a perisomatic compartment and a single dendrite connected to the perisomatic compartment. The perisomatic compartment had a diameter of 15 μm and length of 15 μm. These dimensions were chosen to be similar to the somatic dimensions of mouse CA1 pyramidal neurons. The dendritic section had a diameter of 4 μm and a length of 500 μm. It was divided into 10 compartments (segments in NEURON nomenclature) to make each compartment small enough that d_λ rule is followed. The d_λ rule states that each segment is at most 0.1 times the AC length constant at 100Hz (Hines & Carnevale, 2001). To account for sag and inductance in the subthreshold response of a neuron, we included an HCN channel in the perisomatic compartment. We employed a similar approach as the one described in the previous segment except with a few modeifications. There were 6 free parameters instead of 4 namely - perisomatic compartment RM, perisomatic compartment CM, perisomatic compartment axial resistance (RA), dendritic compartment RM, dendritic compartment CM, and dendritic compartment RA (table 8). The Em and h_Chan_Gbar for the models were taken from the previously generated 1compt models. Instead of using V_{-25} for fitting, we used the corresponding neuron's Rin and tau. Also, unlike for 1compt case, we generated 10 valid models for each neuron (for a total of 130 models) instead of just one valid model due to degeneracy that exists in this case. Many passive parameter combinations can give rise to the same subthreshold features while having considerable differences in their subthreshold impedance profile.

Free parameter (units)	symbol	Lower limit	Upper limit
Perisomatic membrane resistance (Ωm^2)	sm_RM	0	20
Perisomatic membrane capacitance (F/m^2)	sm_CM	0	0.2
Perisomatic axial resistance (Ωm)	sm_RA	0	20

Dendritic membrane resistance (Ωm^2)	dend_RM	0	20
Dendritic membrane capacitance (F/m^2)	dend_CM	0	0.2
Dendritic axial resistance (Ωm)	dend_RA	0	20

Table 8: Free parameters and their ranges for the unbiased stochastic search to generate valid passive ball and stick models and valid impedance amplitude fitted models.

Generating valid subthreshold impedance amplitude profiles matched ball and stick models

The same morphology and fitting procedure as described above was used except the models were fitted to the subthreshold impedance amplitude profile of each of the 13 cells. The resulting models fitted well to both the -25 pA response as well as the subthreshold impedance amplitude profiles of the corresponding neuron. For this case too we generated a single valid model corresponding to each neuron.

Generating valid active model triplets

For the morphology hypothesis, we generated triplets of valid active models. For each neuron, we picked its corresponding 1compt subthreshold model, imp model and one of the ten pas models we generated earlier. We then uniformly sampled Na_T_Gbar and K_DR_Gbar over the range provided in table 9 and incorporated these Gbars into the triplet of subthreshold models. We then checked whether any of these models give suprathreshold features outside the experimental range for freq_0, freq_150, ISIavg_150 and AP1_amp_150 (see table 6 for experimental range). If any, the whole triplet was discarded. We repeated this procedure for a neuron 5000 times. Thus we inspected a total of 13x5000=65000 triplets. A total of 4248 triplets were found to be valid and were used for analysis in Fig5. This procedure allowed us to compare models with the same maximal conductances, and subthreshold features but different impedance amplitude profiles.

Free parameter (units)	symbol	Lower limit	Upper limit
Perisomatic Na_T channel maximal conductance (μS)*	Na_T_Chan_Gbar	0.1	10

Perisomatic K_DR channel maximal conductance (μS)*	K_DR_Chan_Gbar	1	1000

Table 9: Free parameters and their ranges for the unbiased stochastic search to generate active model triplets (1compt, pas and imp). * The Gbars were logarithmically sampled with a base of 10.

Generating models with different K_DR reversal potential

Single compartment models of dimensions 15 μm (length) x 15 μm (diameter) were used. The free parameters and their allowed range are given in Table 10. We used a uniform random distribution to pick the values of these free parameters and recorded their Rin, Cin, E_rest, freq_0, freq_150, and ISIavg_150. Since we were modifying the K_DR Erev to unphysiologically high levels, the validity criteria were a bit relaxed for freq_150, and ISIavg_150. Instead of using the 10-90th percentile experimental range as valid range, we used half the 10th percentile experimental value and double the 90th percentile experimental value as the valid range (see table 6 for 10th and 90th percentile experimental values of the active features). For subthreshold features, the validity criterion was still the same (table 5). If these values were not within experimental range, the model was discarded. We also recorded each valid model's DBLO at 150 pA current injection. We did not include h_Chan in these models.

Out of a total of 5000 models that were inspected, 231 were valid and were used for analysis.

Free parameter (units)	symbol	Lower limit	Upper limit
Reversal potential of leak current (mV)	Em	-100	-70
Perisomatic membrane resistance (Ωm^2)	sm_RM	0.09	0.11
Perisomatic membrane capacitance (F/m^2)	sm_CM	0.085	0.34
Perisomatic Na_T channel maximal conductance (μS)*	Na_T_Chan_Gbar	0.1	10
Perisomatic K_DR channel maximal conductance (μS)*	K_DR_Chan_Gbar	1	1000
Perisomatic K_DR reversal potential (mV)	K_DR_Chan_Erev	-100	-50

Table 10: Free parameters and their ranges for the unbiased stochastic search to generate active models for K_DR Erev hypothesis. Parameters with * were not sampled uniformly but logarithmically with base 10.

Exploring K_DR kinetics space

To build models with different K_DR kinetics, we randomly picked one of the thirteen subthreshold 1compt models we built previously and incorporated Na_T_Chan and K_DR_Chan in those models. The free parameters are provided in table 10. Out of the eight free parameters, six were for the K_DR time constant curve parameterized as in eq {22-24}. These parameters are further explained in Fig 7B and eq {22-24}. We did not vary the steady state inf curve of K_DR. A random number with a uniform distribution between the limits specified in the table was picked for each parameter. The model was then checked whether their freq_150, freq_0, ISIavg_150 and AP1_amp_150 were within experimental range (table 6). This procedure was repeated a total of 50000 times and the generated models were checked for validity. 677 models passed the validity criterion.

Free parameter (units)	symbol	Lower limit	Upper limit
Perisomatic Na_T channel maximal conductance (μS)*	Na_T_Chan_Gbar	0.1	10
Perisomatic K_DR channel maximal conductance (μS)*	K_DR_Chan_Gbar	1	1000
K_DR n_A (au)	n_A	0.0116	0.0136
K_DR n_B (au)	n_B	0.00346	0.0865
K_DR n_C (au)	n_C	0	0.01
K_DR n_D (au)	n_D	0	0.01
K_DR n_E (au)	n_E	0.00686	0.1715
K_DR n_F (au)	n_F	0.02	0.5

Table 11: Free parameters and their ranges for the unbiased stochastic search to explore the K_DR kinetics space.

Models with different Na_T kinetics

For this part, we made three families of models - Gouwens, Migliore and Royeck. For each of these families of models, we first picked one of the 13 subthreshold 1compt models. We then incorporated Na_T and K_DR into those models with their Gbar levels chosen uniformly over the range specified in table 12. For Gouwen models, Na_T kinetics from Gouwens et al., 2018 was used as described in a previous section. For Migliore models, the Na_T kinetics originated from Migliore et al., 2018 while for Royeck models, Na_T kinetics from Royeck et al., 2018 and Hay et al., 2011 were used. Refer to the first section of Materials and Methods for details on the kinetics. The models were then checked if their freq_0, freq_0, and AP1_amp_150, and ISIavg_150 is within experimental range (table 6). Invalid models were discarded. This procedure was repeated 500 times for each subthreshold 1compt model for a total of 13x500=6500 time per model family. For Gouwens models, 406 models were valid. 119 Royeck models were valid while only 24 Migliore models were valid.

Free parameter (units)	symbol	Lower limit	Upper limit
Perisomatic Na_T channel maximal conductance (μS)*	Na_T_Chan_Gbar	1	100
Perisomatic K_DR channel maximal conductance (μS)*	K_DR_Chan_Gbar	0.1	100

Table 12: Free parameters and their ranges for the unbiased stochastic search to generate models with different Na_T kinetics (Gouwens, Royeck and Migliore). * The Gbars were logarithmically sampled with a base of 10.

Generating consolidated models

To generate valid consolidated models, we started with one of the thirteen subthreshold imp models. We incorporated Gouwens et al., 2018 Na_T kinetics and a fast K_DR channel in the model. A depolarized K_DR E_{rev} of -90mV was used in this case. The Gbar value was chosen from a uniform distribution with range specified in table 13. We then checked whether the model's freq_0, freq_150, ISIavg_150, and AP1_amp_150 were within experimental range (table 6). Invalid models were discarded. We repeated the above procedure 5000 times for each subthreshold imp model for a total of 13x5000=65000 models tested. 580 models passed this validity test.

Free parameter (units)	symbol	Lower limit	Upper limit

Perisomatic Na_T channel maximal conductance (μS)*	Na_T_Chan_Gbar	1	100
Perisomatic K_DR channel maximal conductance (μS)*	K_DR_Chan_Gbar	0.1	100

Table 13: Free parameters and their ranges for the unbiased stochastic search to generate consolidated models. *The Gbars were logarithmically sampled with a base of 10.

Bistable models

We first picked one of the 4248 active imp models that were generated previously. We then incorporated Na_P into the model. We then chose a random value of the 4 free parameters as per the range specified in Table 14. The generated models were checked for bistability wherein a 150pA current was injected between 500 and 1000 ms, and a -50 pA current was injected between 1500 and 2000 ms. The stimulus period ended with zero current injection in the last 500 ms. This procedure was repeated 400,000 times. The criterion for bistability was at most one AP in the first 0 pA window (to allow the model to settle), tonic firing during the 150 pA window, at least two APs during the second 0 pA window, at most one spike for the -50 pA window (to allow for rebound spiking), and lastly no spiking in the last 0 pA window. All 14 models that met these criteria for bistability had high DBLO.

Free parameter (units)	symbol	Lower limit	Upper limit
Perisomatic Na_P channel maximal conductance (μS)*	Na_P_Chan_Gbar	1e-5	0.1
Perisomatic Na_P channel inf curve half activation voltage (mV)	Na_P_Chan_mvhalf	-80	-50
Perisomatic Na_P channel inf curve slope at half activation voltage (mV)	Na_P_Chan_mvslope	2	15
Perisomatic membrane resistance (Ωm^2)*	sm_RM	0.1	20

Table 14: Free parameters and their ranges for the unbiased stochastic search to explore the role of Na_P in firing bistability. *These were logarithmically sampled with a base of 10.

Acknowledgements

NCBS-TIFR receives the support of the Department of Atomic Energy, Government of India, under Project Identification No. RTI 4006. We thank Sufyan Ashhad for their valuable suggestions especially regarding the role of reversal potential of K_DR. We also thank Rishikesh Narayanan for their useful suggestions on the project.

Author contributions

AK performed the simulations and wrote the paper. AKS performed the experiments and wrote the corresponding methods section. USB supervised the project, obtained funds, and wrote the paper.

Data and Model availability

All data, models and code used in this work are available on the github repository https://github.com/BhallaLab/DBLO_paper/tree/main. The models are also available on ModelDB with accession number [].

References

Action potential. (2023). In *Wikipedia*.

https://en.wikipedia.org/w/index.php?title=Action_potential&oldid=1184911660

Alam, S. R., Bartolome, J., Carpene, M., Happonen, K., Lafoucriere, J.-C., & Pleiter, D. (2022). Fenix: A Pan-European federation of supercomputing and cloud e-infrastructure services. *Communications of the ACM*, *65*(4), 46–47. https://doi.org/10.1145/3511802

Alejandre-García, T., Kim, S., Pérez-Ortega, J., & Yuste, R. (2022). Intrinsic excitability mechanisms of neuronal ensemble formation. *eLife*, *11*, e77470. https://doi.org/10.7554/eLife.77470

Ascoli, G. A., Donohue, D. E., & Halavi, M. (2007). NeuroMorpho.Org: A Central Resource for Neuronal Morphologies. *Journal of Neuroscience*, *27*(35), 9247–9251. https://doi.org/10.1523/JNEUROSCI.2055-07.2007

Atallah, B. V., & Scanziani, M. (2009). Instantaneous Modulation of Gamma Oscillation Frequency by Balancing Excitation with Inhibition. *Neuron*, *62*(4), 566–577. https://doi.org/10.1016/j.neuron.2009.04.027

Barmashenko, G., Hefft, S., Aertsen, A., Kirschstein, T., & Köhling, R. (2011). Positive shifts of the GABAA receptor reversal potential due to altered chloride homeostasis is widespread after status epilepticus. *Epilepsia*, *52*(9), 1570–1578. https://doi.org/10.1111/j.1528-1167.2011.03247.x

Bekkers, J. M., & Häusser, M. (2007). Targeted dendrotomy reveals active and passive contributions of the dendritic tree to synaptic integration and neuronal output. *Proceedings of the National Academy of Sciences*, *104*(27), 11447–11452. https://doi.org/10.1073/pnas.0701586104

Bianchi, D., Migliore, R., Vitale, P., Garad, M., Pousinha, P. A., Marie, H., Lessmann, V., & Migliore, M. (2022). Membrane electrical properties of mouse hippocampal CA1 pyramidal neurons during strong inputs. *Biophysical Journal*, *121*(4), 644–657. https://doi.org/10.1016/j.bpj.2022.01.002

Binini, N., Talpo, F., Spaiardi, P., Maniezzi, C., Pedrazzoli, M., Raffin, F., Mattiello, N., Castagno, A. N., Masetto, S., Yanagawa, Y., Dickson, C. T., Ramat, S., Toselli, M., & Biella, G. R. (2021). Membrane Resonance in Pyramidal and GABAergic Neurons of the Mouse Perirhinal Cortex. *Frontiers in Cellular Neuroscience*, *15*. https://www.frontiersin.org/articles/10.3389/fncel.2021.703407

Brown, H. F., Difrancesco, D., & Noble, S. J. (1979). How does adrenaline accelerate the heart? *Nature*, *280*(5719), Article 5719. https://doi.org/10.1038/280235a0

Carnevale, N. T., & Hines, M. L. (2006). *The NEURON Book* (1st ed.). Cambridge University Press. https://doi.org/10.1017/CBO9780511541612

Colbert, C. M., & Johnston, D. (1996). Axonal Action-Potential Initiation and Na+ Channel Densities in the Soma and Axon Initial Segment of Subicular Pyramidal Neurons. *Journal*

of Neuroscience, *16*(21), 6676–6686. https://doi.org/10.1523/JNEUROSCI.16-21-06676.1996

Colbert, C. M., & Pan, E. (2002). Ion channel properties underlying axonal action potential initiation in pyramidal neurons. *Nature Neuroscience*, *5*(6), 533–538. https://doi.org/10.1038/nn0602-857

Dhupia, N., Rathour, R. K., & Narayanan, R. (2015). Dendritic atrophy constricts functional maps in resonance and impedance properties of hippocampal model neurons. *Frontiers in Cellular Neuroscience*, *8*. https://www.frontiersin.org/articles/10.3389/fncel.2014.00456

Doya, K. (2002). Metalearning and neuromodulation. *Neural Networks*, *15*(4), 495–506. https://doi.org/10.1016/S0893-6080(02)00044-8

Dwivedi, D., Chattarji, S., & Bhalla, U. S. (2019). Impaired Reliability and Precision of Spiking in Adults But Not Juveniles in a Mouse Model of Fragile X Syndrome. *eNeuro*, *6*(6). https://doi.org/10.1523/ENEURO.0217-19.2019

Eppler, J., Helias, M., Muller, E., Diesmann, M., & Gewaltig, M.-O. (2009). PyNEST: A convenient interface to the NEST simulator. *Frontiers in Neuroinformatics*, *2*. https://www.frontiersin.org/articles/10.3389/neuro.11.012.2008

Fadool, D. A., Tucker, K., & Pedarzani, P. (2011). Mitral Cells of the Olfactory Bulb Perform Metabolic Sensing and Are Disrupted by Obesity at the Level of the Kv1.3 Ion Channel. *PLOS ONE*, *6*(9), e24921. https://doi.org/10.1371/journal.pone.0024921

Fuentealba, P., Timofeev, I., Bazhenov, M., Sejnowski, T. J., & Steriade, M. (2005). Membrane Bistability in Thalamic Reticular Neurons During Spindle Oscillations. *Journal of Neurophysiology*, *93*(1), 294–304. https://doi.org/10.1152/jn.00552.2004

Golomb, D., Shedmi, A., Curtu, R., & Ermentrout, G. B. (2006). Persistent Synchronized Bursting Activity in Cortical Tissues With Low Magnesium Concentration: A Modeling Study. *Journal of Neurophysiology*, *95*(2), 1049–1067. https://doi.org/10.1152/jn.00932.2005

Golowasch, J. (2019). Neuromodulation of central pattern generators and its role in the functional recovery of central pattern generator activity. *Journal of Neurophysiology*, *122*(1), 300–315. https://doi.org/10.1152/jn.00784.2018

Goodman, D., & Brette, R. (2008). Brian: A simulator for spiking neural networks in Python. *Frontiers in Neuroinformatics*, *2*. https://www.frontiersin.org/articles/10.3389/neuro.11.005.2008

Gouwens, N. W., Berg, J., Feng, D., Sorensen, S. A., Zeng, H., Hawrylycz, M. J., Koch, C., & Arkhipov, A. (2018). Systematic generation of biophysically detailed models for diverse cortical neuron types. *Nature Communications*, *9*(1), Article 1. https://doi.org/10.1038/s41467-017-02718-3

Gutierrez, G. J., & Marder, E. (2014). Modulation of a Single Neuron Has State-Dependent Actions on Circuit Dynamics. *eNeuro*, *1*(1). https://doi.org/10.1523/ENEURO.0009-14.2014

Hay, E., Hill, S., Schürmann, F., Markram, H., & Segev, I. (2011). Models of Neocortical Layer 5b Pyramidal Cells Capturing a Wide Range of Dendritic and Perisomatic Active Properties. *PLOS Computational Biology*, *7*(7), e1002107. https://doi.org/10.1371/journal.pcbi.1002107

Hendrickson, E. B., Edgerton, J. R., & Jaeger, D. (2011). The capabilities and limitations of conductance-based compartmental neuron models with reduced branched or unbranched morphologies and active dendrites. *Journal of Computational Neuroscience*, *30*(2), 301–321. https://doi.org/10.1007/s10827-010-0258-z

Hess, S., Pouzat, C., Paeger, L., Pippow, A., & Kloppenburg, P. (2021). Analysis of neuronal Ca2+ handling properties by combining perforated patch clamp recordings and the added buffer approach. *Cell Calcium*, *97*, 102411. https://doi.org/10.1016/j.ceca.2021.102411

Hines, M. L., & Carnevale, N. T. (2001). Neuron: A Tool for Neuroscientists. *The Neuroscientist*,

7(2), 123–135. https://doi.org/10.1177/107385840100700207

Hodgkin, A. L., & Huxley, A. F. (1952). A quantitative description of membrane current and its application to conduction and excitation in nerve. *The Journal of Physiology*, *117*(4), 500–544. https://doi.org/10.1113/jphysiol.1952.sp004764

Hunt, D. L., Linaro, D., Si, B., Romani, S., & Spruston, N. (2018). A novel pyramidal cell type promotes sharp-wave synchronization in the hippocampus. *Nature Neuroscience*, *21*(7), Article 7. https://doi.org/10.1038/s41593-018-0172-7

Jepma, M., Murphy, P. R., Nassar, M. R., Rangel-Gomez, M., Meeter, M., & Nieuwenhuis, S. (2016). Catecholaminergic Regulation of Learning Rate in a Dynamic Environment. *PLOS Computational Biology*, *12*(10), e1005171. https://doi.org/10.1371/journal.pcbi.1005171

Kandel, E. R., Koester, J., Mack, S., & Siegelbaum, S. (Eds.). (2021). *Principles of neural science* (Sixth edition). McGraw Hill.

Kim, E. J., Juavinett, A. L., Kyubwa, E. M., Jacobs, M. W., & Callaway, E. M. (2015). Three Types of Cortical Layer 5 Neurons That Differ in Brain-wide Connectivity and Function. *Neuron*, *88*(6), 1253–1267. https://doi.org/10.1016/j.neuron.2015.11.002

Kole, M. H. P., Ilschner, S. U., Kampa, B. M., Williams, S. R., Ruben, P. C., & Stuart, G. J. (2008). Action potential generation requires a high sodium channel density in the axon initial segment. *Nature Neuroscience*, *11*(2), Article 2. https://doi.org/10.1038/nn2040

Lundqvist, M., Compte, A., & Lansner, A. (2010). Bistable, Irregular Firing and Population Oscillations in a Modular Attractor Memory Network. *PLOS Computational Biology*, *6*(6), e1000803. https://doi.org/10.1371/journal.pcbi.1000803

Magee, J. C., & Johnston, D. (1995). Characterization of single voltage-gated Na+ and Ca2+ channels in apical dendrites of rat CA1 pyramidal neurons. *The Journal of Physiology*, *487*(1), 67–90. https://doi.org/10.1113/jphysiol.1995.sp020862

Marder, E., O'Leary, T., & Shruti, S. (2014). Neuromodulation of Circuits with Variable

Parameters: Single Neurons and Small Circuits Reveal Principles of State-Dependent and Robust Neuromodulation. *Annual Review of Neuroscience*, *37*(1), 329–346. https://doi.org/10.1146/annurev-neuro-071013-013958

Marino, M., Misuri, L., & Brogioli, D. (2014). *A new open source software for the calculation of the liquid junction potential between two solutions according to the stationary Nernst-Planck equation* (arXiv:1403.3640). arXiv. https://doi.org/10.48550/arXiv.1403.3640

Martina, M., Schultz, J. H., Ehmke, H., Monyer, H., & Jonas, P. (1998). Functional and Molecular Differences between Voltage-Gated K+ Channels of Fast-Spiking Interneurons and Pyramidal Neurons of Rat Hippocampus. *Journal of Neuroscience*, *18*(20), 8111–8125. https://doi.org/10.1523/JNEUROSCI.18-20-08111.1998

McDougal, R. A., Morse, T. M., Carnevale, T., Marenco, L., Wang, R., Migliore, M., Miller, P. L., Shepherd, G. M., & Hines, M. L. (2017). Twenty years of ModelDB and beyond: Building essential modeling tools for the future of neuroscience. *Journal of Computational Neuroscience*, *42*(1), 1–10. https://doi.org/10.1007/s10827-016-0623-7

Metz, A. E., Jarsky, T., Martina, M., & Spruston, N. (2005). R-Type Calcium Channels Contribute to Afterdepolarization and Bursting in Hippocampal CA1 Pyramidal Neurons. *Journal of Neuroscience*, *25*(24), 5763–5773. https://doi.org/10.1523/JNEUROSCI.0624-05.2005

Migliore, M., Hoffman, D. A., Magee, J. C., & Johnston, D. (1999). Role of an A-Type K+ Conductance in the Back-Propagation of Action Potentials in the Dendrites of Hippocampal Pyramidal Neurons. *Journal of Computational Neuroscience*, *7*(1), 5–15. https://doi.org/10.1023/A:1008906225285

Migliore, R., Lupascu, C. A., Bologna, L. L., Romani, A., Courcol, J.-D., Antonel, S., Geit, W. A. H. V., Thomson, A. M., Mercer, A., Lange, S., Falck, J., Rössert, C. A., Shi, Y., Hagens, O., Pezzoli, M., Freund, T. F., Kali, S., Muller, E. B., Schürmann, F., … Migliore, M. (2018). The physiological variability of channel density in hippocampal CA1 pyramidal

cells and interneurons explored using a unified data-driven modeling workflow. *PLOS Computational Biology*, *14*(9), e1006423. https://doi.org/10.1371/journal.pcbi.1006423

Miyasho, T., Takagi, H., Suzuki, H., Watanabe, S., Inoue, M., Kudo, Y., & Miyakawa, H. (2001). Low-threshold potassium channels and a low-threshold calcium channel regulate Ca2+ spike firing in the dendrites of cerebellar Purkinje neurons: A modeling study. *Brain Research*, *891*(1–2), 106–115. https://doi.org/10.1016/S0006-8993(00)03206-6

Moberg, S., & Takahashi, N. (2022). Neocortical layer 5 subclasses: From cellular properties to roles in behavior. *Frontiers in Synaptic Neuroscience*, *14*. https://www.frontiersin.org/articles/10.3389/fnsyn.2022.1006773

Moore, S. J., Cooper, D. C., & Spruston, N. (2009). Plasticity of Burst Firing Induced by Synergistic Activation of Metabotropic Glutamate and Acetylcholine Receptors. *Neuron*, *61*(2), 287–300. https://doi.org/10.1016/j.neuron.2008.12.013

Moradi Chameh, H., Rich, S., Wang, L., Chen, F.-D., Zhang, L., Carlen, P. L., Tripathy, S. J., & Valiante, T. A. (2021). Diversity amongst human cortical pyramidal neurons revealed via their sag currents and frequency preferences. *Nature Communications*, *12*(1), Article 1. https://doi.org/10.1038/s41467-021-22741-9

Müller, P., Draguhn, A., & Egorov, A. V. (2018). Persistent sodium current modulates axonal excitability in CA1 pyramidal neurons. *Journal of Neurochemistry*, *146*(4), 446–458. https://doi.org/10.1111/jnc.14479

Nadim, F., & Bucher, D. (2014). Neuromodulation of neurons and synapses. *Current Opinion in Neurobiology*, *29*, 48–56. https://doi.org/10.1016/j.conb.2014.05.003

Narayanan, R., & Johnston, D. (2007). Long-Term Potentiation in Rat Hippocampal Neurons Is Accompanied by Spatially Widespread Changes in Intrinsic Oscillatory Dynamics and Excitability. *Neuron*, *56*(6), 1061–1075. https://doi.org/10.1016/j.neuron.2007.10.033

Neher, E. (1992). [6] Correction for liquid junction potentials in patch clamp experiments. In *Methods in Enzymology* (Vol. 207, pp. 123–131). Academic Press.

https://doi.org/10.1016/0076-6879(92)07008-C

Owens, D. F., & Kriegstein, A. R. (2002). Is there more to gaba than synaptic inhibition? *Nature Reviews Neuroscience*, *3*(9), Article 9. https://doi.org/10.1038/nrn919

Palacios-Filardo, J., & Mellor, J. R. (2019). Neuromodulation of hippocampal long-term synaptic plasticity. *Current Opinion in Neurobiology*, *54*, 37–43. https://doi.org/10.1016/j.conb.2018.08.009

Pawelzik, H., Hughes, D. I., & Thomson, A. M. (2003). Modulation of inhibitory autapses and synapses on rat CA1 interneurones by GABA $_a$ receptor ligands. *The Journal of Physiology*, *546*(3), 701–716. https://doi.org/10.1113/jphysiol.2002.035121

Peerboom, C., & Wierenga, C. J. (2021). The postnatal GABA shift: A developmental perspective. *Neuroscience & Biobehavioral Reviews*, *124*, 179–192. https://doi.org/10.1016/j.neubiorev.2021.01.024

Podlaski, W. F., Seeholzer, A., Groschner, L. N., Miesenböck, G., Ranjan, R., & Vogels, T. P. (2017). Mapping the function of neuronal ion channels in model and experiment. *eLife*, *6*, e22152. https://doi.org/10.7554/eLife.22152

Protachevicz, P. R., Borges, F. S., Lameu, E. L., Ji, P., Iarosz, K. C., Kihara, A. H., Caldas, I. L., Szezech, J. D., Baptista, M. S., Macau, E. E. N., Antonopoulos, C. G., Batista, A. M., & Kurths, J. (2019). Bistable Firing Pattern in a Neural Network Model. *Frontiers in Computational Neuroscience*, *13*. https://www.frontiersin.org/articles/10.3389/fncom.2019.00019

Quraishi, I. H., Stern, S., Mangan, K. P., Zhang, Y., Ali, S. R., Mercier, M. R., Marchetto, M. C., McLachlan, M. J., Jones, E. M., Gage, F. H., & Kaczmarek, L. K. (2019). An Epilepsy-Associated KCNT1 Mutation Enhances Excitability of Human iPSC-Derived Neurons by Increasing Slack KNa Currents. *Journal of Neuroscience*, *39*(37), 7438–7449. https://doi.org/10.1523/JNEUROSCI.1628-18.2019

Rall, W. (1969). Time Constants and Electrotonic Length of Membrane Cylinders and Neurons.

Biophysical Journal, *9*(12), 1483–1508. https://doi.org/10.1016/S0006-3495(69)86467-2

Ranjan, R., Khazen, G., Gambazzi, L., Ramaswamy, S., Hill, S., Schürmann, F., & Markram, H. (2011). Channelpedia: An Integrative and Interactive Database for Ion Channels. *Frontiers in Neuroinformatics*, *5*. https://www.frontiersin.org/articles/10.3389/fninf.2011.00036

Ranjan, R., Van Geit, W., Moor, R., Rössert, C., Riquelme, J. L., Damart, T., Jaquier, A., & Tuncel, A. (2024). *eFEL* (5.5.1) [Computer software]. Zenodo. https://doi.org/10.5281/zenodo.10492799

Ray, S., & Bhalla, U. (2008). PyMOOSE: Interoperable scripting in Python for MOOSE. *Frontiers in Neuroinformatics*, *2*. https://www.frontiersin.org/articles/10.3389/neuro.11.006.2008

Roy, R., & Narayanan, R. (2023). Ion-channel degeneracy and heterogeneities in the emergence of complex spike bursts in CA3 pyramidal neurons. *The Journal of Physiology*, *601*(15), 3297–3328. https://doi.org/10.1113/JP283539

Royeck, M., Horstmann, M.-T., Remy, S., Reitze, M., Yaari, Y., & Beck, H. (2008). Role of Axonal NaV1.6 Sodium Channels in Action Potential Initiation of CA1 Pyramidal Neurons. *Journal of Neurophysiology*, *100*(4), 2361–2380. https://doi.org/10.1152/jn.90332.2008

Rutledge, R. B., Lazzaro, S. C., Lau, B., Myers, C. E., Gluck, M. A., & Glimcher, P. W. (2009). Dopaminergic Drugs Modulate Learning Rates and Perseveration in Parkinson's Patients in a Dynamic Foraging Task. *Journal of Neuroscience*, *29*(48), 15104–15114. https://doi.org/10.1523/JNEUROSCI.3524-09.2009

Sahu, G., Asmara, H., Zhang, F.-X., Zamponi, G. W., & Turner, R. W. (2017). Activity-Dependent Facilitation of CaV1.3 Calcium Channels Promotes KCa3.1 Activation in Hippocampal Neurons. *Journal of Neuroscience*, *37*(46), 11255–11270. https://doi.org/10.1523/JNEUROSCI.0967-17.2017

Sahu, G., Wazen, R.-M., Colarusso, P., Chen, S. R. W., Zamponi, G. W., & Turner, R. W. (2019). Junctophilin Proteins Tether a Cav1-RyR2-KCa3.1 Tripartite Complex to Regulate

Neuronal Excitability. *Cell Reports*, *28*(9), 2427-2442.e6. https://doi.org/10.1016/j.celrep.2019.07.075

Staff, N. P., Jung, H.-Y., Thiagarajan, T., Yao, M., & Spruston, N. (2000). Resting and Active Properties of Pyramidal Neurons in Subiculum and CA1 of Rat Hippocampus. *Journal of Neurophysiology*, *84*(5), 2398–2408. https://doi.org/10.1152/jn.2000.84.5.2398

Studtmann, C., Ladislav, M., Safari, M., Khondaker, R., Chen, Y., Vaughan, G. A., Topolski, M. A., Tomović, E., Balík, A., & Swanger, S. A. (2023). Ventral posterolateral and ventral posteromedial thalamocortical neurons have distinct physiological properties. *Journal of Neurophysiology*, *130*(6), 1492–1507. https://doi.org/10.1152/jn.00525.2022

Szabó, G. G., Holderith, N., Gulyás, A. I., Freund, T. F., & Hájos, N. (2010). Distinct synaptic properties of perisomatic inhibitory cell types and their different modulation by cholinergic receptor activation in the CA3 region of the mouse hippocampus. *European Journal of Neuroscience*, *31*(12), 2234–2246. https://doi.org/10.1111/j.1460-9568.2010.07292.x

Tang, L. S., Goeritz, M. L., Caplan, J. S., Taylor, A. L., Fisek, M., & Marder, E. (2010). Precise Temperature Compensation of Phase in a Rhythmic Motor Pattern. *PLOS Biology*, *8*(8), e1000469. https://doi.org/10.1371/journal.pbio.1000469

Tomko, M., Benuskova, L., & Jedlicka, P. (2021). A new reduced-morphology model for CA1 pyramidal cells and its validation and comparison with other models using HippoUnit. *Scientific Reports*, *11*(1), 7615. https://doi.org/10.1038/s41598-021-87002-7

Turi, G. F., Li, W.-K., Chavlis, S., Pandi, I., O'Hare, J., Priestley, J. B., Grosmark, A. D., Liao, Z., Ladow, M., Zhang, J. F., Zemelman, B. V., Poirazi, P., & Losonczy, A. (2019). Vasoactive Intestinal Polypeptide-Expressing Interneurons in the Hippocampus Support Goal-Oriented Spatial Learning. *Neuron*, *101*(6), 1150-1165.e8. https://doi.org/10.1016/j.neuron.2019.01.009

Turner, D. A., & Schwartzkroin, P. A. (1983). Electrical characteristics of dendrites and dendritic spines in intracellularly stained CA3 and dentate hippocampal neurons. *Journal of*

Neuroscience, *3*(11), 2381–2394. https://doi.org/10.1523/JNEUROSCI.03-11-02381.1983

Vallat, R. (2018). Pingouin: Statistics in Python. *Journal of Open Source Software*, *3*(31), 1026. https://doi.org/10.21105/joss.01026

Virtanen, P., Gommers, R., Oliphant, T. E., Haberland, M., Reddy, T., Cournapeau, D., Burovski, E., Peterson, P., Weckesser, W., Bright, J., van der Walt, S. J., Brett, M., Wilson, J., Millman, K. J., Mayorov, N., Nelson, A. R. J., Jones, E., Kern, R., Larson, E., … van Mulbregt, P. (2020). SciPy 1.0: Fundamental algorithms for scientific computing in Python. *Nature Methods*, *17*(3), Article 3. https://doi.org/10.1038/s41592-019-0686-2

Williams, A. H., Hamood, A. W., & Marder, E. (2022). Neuromodulation in Small Networks. In D. Jaeger & R. Jung (Eds.), *Encyclopedia of Computational Neuroscience* (pp. 2300–2313). Springer. https://doi.org/10.1007/978-1-0716-1006-0_26

Yu, Y., Migliore, M., Hines, M. L., & Shepherd, G. M. (2014). Sparse Coding and Lateral Inhibition Arising from Balanced and Unbalanced Dendrodendritic Excitation and Inhibition. *Journal of Neuroscience*, *34*(41), 13701–13713. https://doi.org/10.1523/JNEUROSCI.1834-14.2014

Zielen, A. J. (1963). THE ELIMINATION OF LIQUID JUNCTION POTENTIALS WITH THE GLASS ELECTRODE. *The Journal of Physical Chemistry*, *67*(7), 1474–1479. https://doi.org/10.1021/j100801a018